Dynamics of undulatory fluctuations of semiflexible filaments in a network

Jonathan Kernes[1] and Alex J. Levine[1,2,3]
[1]*Department of Physics and Astronomy, UCLA, Los Angeles, California 90095, USA*
[2]*Department of Chemistry and Biochemistry, UCLA, Los Angeles, California 90095, USA*
[3]*Department of Computational Medicine, UCLA, Los Angeles, California 90095, USA*

(Received 18 June 2020; accepted 30 October 2020; published 3 December 2020)

We study the dynamics of a single semiflexible filament coupled to a Hookean spring at its boundary. The spring produces a fluctuating tensile force on the filament, the value of which depends on the filament's instantaneous end-to-end length. The spring thereby introduces a nonlinearity, which mixes the undulatory normal modes of the filament and changes their dynamics. We study these dynamics using the Martin–Siggia–Rose–Janssen–De Dominicis formalism, and compute the time-dependent correlation functions of transverse undulations and of the filament's end-to-end distance. The relaxational dynamics of the modes below a characteristic wavelength $\sqrt{\kappa/\tau_R}$, set by the filament's bending modulus κ and spring-renormalized tension τ_R, are changed by the boundary spring. This occurs near the crossover frequency between tension- and bending-dominated modes of the system. The boundary spring can be used to represent the linear elastic compliance of the rest of the filament network to which the filament is cross linked. As a result, we predict that this nonlinear effect will be observable in the dynamical correlations of constituent filaments of networks and in the networks' collective shear response. The system's dynamic shear modulus is predicted to exhibit the well-known crossover with increasing frequency from $\omega^{1/2}$ to $\omega^{3/4}$, but the inclusion of the network's compliance in the analysis of the individual filament dynamics shifts this transition to a higher frequency.

DOI: 10.1103/PhysRevE.102.062406

I. INTRODUCTION

Semiflexible filament networks underlie the structure of a number of biological materials, including the cytoskeleton and the extracellular matrix of tissues [1–3]. The mechanical properties of such materials depend on the mechanics of their individual filaments. These semiflexible filaments are essentially inextensible, with lengths less than their thermal persistence length, indicating a large bending rigidity κ that keeps them oriented along a mean direction.

Filamentous networks exhibit a number of interesting mechanical properties that differ from typical elastic continua, such as nonaffine deformation [4,5] and negative normal stress [6,7]. There is now a well-developed theory connecting the tension response of individual filaments to the linear collective shear response of their networks: $G(\omega)$. Due to the appearance of multiple time scales in the networks' dynamics, $G(\omega)$ exhibits a rich variety of behaviors [8–11].

There is currently considerable interest in local microrheological probes of tension within the network at the single filament scale. This approach allows one to noninvasively measure tension in the constituent filaments of a semiflexible network by measuring their fluctuation spectrum. This probe is predicated on the idea that tension applied to a filament segment changes the thermal fluctuation spectrum of the filament's transverse undulations. The idea of using the measured thermal fluctuations to map out the tension in a network has been termed *activity microscopy* [12,13]. These tension maps are likely to prove quite interesting in light of the breakdown of continuum mechanics on mesoscopic scales, resulting in force chains appearing in the network near the point of force application [14–17]. In order to better understand the transverse undulation spectrum of filaments within a network, one should account for the fact that this spectrum is controlled in part by the filament's mechanical boundary conditions, due to its coupling to the rest of the network. For example, the fluctuations of the (red) filament in Fig. 1 are modified by that filament's mechanical coupling via cross links (black/gray circles) to the surrounding network of (blue) filaments. These boundary conditions include not only the tension imposed on the filament (the goal of activity microscopy), but also the elastic compliance of the surrounding material.

In our previous paper [13], we examined how the surrounding network, including its elastic compliance and state of tension, affects the equilibrium fluctuation spectrum of the transverse undulations of a constituent filament in the network. In this paper, we expand our analysis to dynamics, looking at the time-dependent correlation and response functions of both individual transverse modes of the filament and the filament's end-to-end distance. In addition to completing the analysis of these boundary conditions on the undulation spectrum by exploring their equilibrium dynamics, these results may be important for interpreting future studies on the frequency-dependent *nonequilibrium* fluctuations of network filament segments driven by endogenous molecular motors [18–21] in a nonequilibrium extension of activity microscopy.

We model the mechanical boundary conditions on the semiflexible filament by both a mean state of tension τ and a linear elastic compliance, representing the surrounding

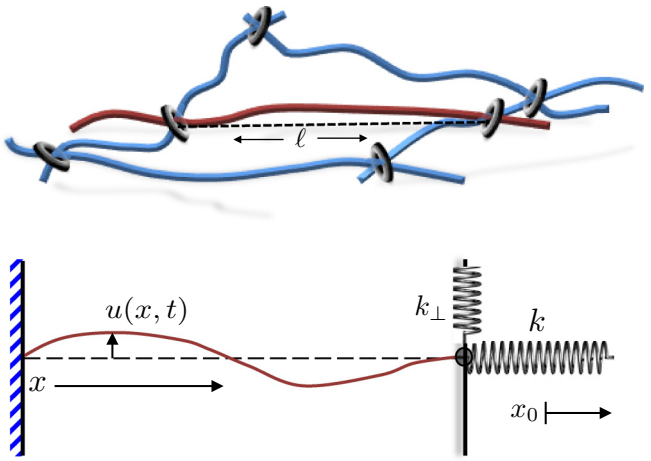

FIG. 1. Top: Visualization of a particular filament (red) cross linked into a network of similar filaments (blue). The cross links are represented by black and gray rings. Bottom: Schematic diagram of a single semiflexible filament. The left end point is pinned, and the right end point is attached to a longitudinal spring with spring constant k and a transverse spring with spring constant $k_\perp$. These represent the elastic compliance of the network. We focus on the effect of the longitudinal spring. Both end points are subject to torque-free boundary conditions.

network. This elastic compliance may be thought of as attaching the filament's end to a pair of Hookean springs, one longitudinal spring aligned with the mean extension of the filament and one perpendicular to it. These springs have spring constants k and $k_\perp$, respectively. The lower panel of Fig. 1 shows a schematic illustration of the system, the dynamics of which will be the focus of this paper. This set of orthogonal springs provides a description of the mechanical compliance of the surrounding network acting on the cross link at the filament's end. Since these springs reflect the linear response of the surrounding network, they are related to its bulk mechanics (shear and compression moduli of the network), but we do not investigate that further here.

The effect of the two springs on the filament's fluctuation spectrum are actually quite distinct. The perpendicular spring changes the spatial structure of the eigenmodes of filament deformation (see Appendix D). The longitudinal spring is the most interesting, as it introduces a nonlinearity into the filament's Hamiltonian even in the limit of small bending. The origin of this nonlinearity (explained more fully below and in Ref. [13]) is that the state of tension in the filament depends on the instantaneous projected length of the filament. Since we work in the limit that the filament is inextensible, tension propagation is instantaneous, and the longitudinal spring introduces a term that is nondiagonal in the Fourier modes of the filament's undulations, but local in time. As a result of this nonlinearity, the equilibrium fluctuation spectrum [13] of the filament and its dynamics are controlled by the set of parameters (κ, τ, k).

The nonlinearity introduced by the boundary compliance (due to the rest of the network) alters the power spectrum of the variations of the projected length of a filament's end-to-end distance when it is cross linked into a network. We study that here. Using our model, we also calculate the response of that distance to applied forces. The time-dependent, single-filament response can be then be used to calculate the dynamic shear modulus and compliance of the network by well-known methods [9]. The most direct experimental test of our theory, however, is to be found at the single filament level. We propose that one can directly measure the relaxational dynamics of a single filament anchored to a substrate and attached to a bead held in an optical trap [22–24]. In such a configuration, the trap provides a longitudinal spring of known (in principle) spring constant. By moving the trap's center, one can measure the changes in filament's fluctuations as a function of tension. In addition to passive measurements, one should also be able to actively measure the response function of the filament's end-to-end distance by driving it via the sinusoidal oscillations of the trap's center. We predict that the new effect associated with the elastic compliance of the trap will be most evident at small values of applied tension.

The remainder of this paper is organized as follows. We introduce the model, including the stochastic equation of motion (Langevin equation) of the filament using slender body dynamics, in Sec. II A. Due to the nonlinearity in the Hamiltonian, we cannot solve these dynamical equations exactly. Instead, in Sec. III we first compute the linear response to transverse applied loads in the wave-number domain to second order in the longitudinal spring constant. From this, we determine the dynamical two-point function $\langle |u_p(\omega)|^2 \rangle$ in Fourier space. These perturbative calculations are organized using the Martin–Siggia–Rose–Janssen–De Dominicis (MSRJD) functional integral formalism [25]. Within this diagrammatic expansion, we comment on various classes of diagrams and propose an approximation using a resummation of the dominant terms of the perturbation series.

To make these approximations precise, we develop an effective field theory (in Sec. IV), the mean-field solution of which reproduces the resummation of the dominant terms. The mean-field solution is a type of dynamical self-consistent theory, which we analyze in Sec. IV A. This self-consistent approach allows us to explore nonequilibrium dynamics and the time-dependent response of pulled filaments. In Sec. IV B we expand our effective field theory about its mean-field solution, allowing us to compute fluctuations, particularly of normal modes and the filament's projected length. These corrections are found to be rooted diagrammatically in the random phase approximation (RPA) borrowed from solid state physics. By considering the terms arising at higher orders in the expansion about the mean field, we identify the various classes of diagrams postulated from the second-order perturbative result, thus determining the validity of our initial approximations. We conclude with a discussion of our results in Sec. V, where we discuss the expected experimental signature of the filament's mechanical boundary conditions on its dynamics. The reader interested primarily in those predictions is encouraged to turn first to that section.

We find two principal effects of the longitudinal spring. The primary one is a renormalization of the tension by the mean force of the spring, which can be schematically viewed as $\tau \to \tau + k\langle \Delta \ell \rangle$. Even if one tunes the applied tension to a small value, the spring, responding to the fluctuations of the end-to-end filament distance, will impose a tension on its own. The spring thus adds an additional energy scale that competes

with the work done by the imposed tension. For small externally applied tension τ ($\tau \ll \kappa^2/k_BT\ell^4$), we can approximate the spring-induced tension by using the spring-free result for the filament arc length taken up in thermal undulations: $\langle \Delta\ell^{\rm free}\rangle = k_BT\ell^2/12\kappa$. There are linear in tension corrections to this result that are well known (see Ref. [26]). Using this approximation, we find that the longitudinal spring constant makes a significant change to the effective tension when k reaches at least $k = k^* \approx 12\kappa\tau/k_BT\ell^2$. Secondly, the nonlinearity generically reduces the effective longitudinal spring constant k, as a result of the nonlinearity transferring the elastic energy amongst the normal modes of filament deformation to a more energetically favorable configuration. This effect is primarily seen in the dynamical projected length fluctuations. At high frequencies, this effect goes away so that the bare spring constant once again becomes observable.

II. FILAMENT DYNAMICS

A. The model

The filament Hamiltonian with the spring-induced nonlinearity was discussed earlier [13], but we briefly reintroduce it here. Since the filament of length ℓ is assumed to be nearly straight, we work in a Monge representation, omitting overhangs, so we may specify the filament's configuration by its transverse coordinate $u(x)$ at a distance x along the mean orientation. Here we work in two dimensions, with the understanding that in three dimensions the dynamics simply involves two copies of the fluctuations considered here, one for each polarization state of the undulations. Where necessary, we later mention the inclusion of both transverse degrees of freedom. We treat the filament as being inextensible. Tension propagation is instantaneous. The change in the filament's projected length due to bending is given to quadratic order in the transverse displacement by

$$\Delta\ell = \frac{1}{2}\int_0^\ell (\partial_x u)^2 dx. \tag{1}$$

The Hamiltonian of the filament with bending rigidity κ, under tension τ, and coupled to a longitudinal spring with spring constant k is

$$H = \frac{\kappa}{2}\int_0^\ell dx\left(\partial_x^2 u\right)^2 + \tau\Delta\ell + \frac{1}{2}k\Delta\ell^2, \tag{2}$$

where $\Delta\ell$ is the amount of the length of the filament taken up by its undulations [see Eq. (1)]. For notational convenience, the spring constant k used here is equal to $4k$ in Ref. [13]. The first term is the usual wormlike chain model, with the restriction of no overhangs. The second term represents the contribution due to tension. The third term is due to to a Hookean spring at the boundary. Since $\Delta\ell$ depends quadratically on the normal modes of the filament, this final term is nonlinear. Though the nonlinearity was introduced via a boundary condition (coupling the filament to a longitudinal spring), it manifests as a contribution to the bulk Hamiltonian.

The tension $\tau = \tau_{\rm applied} + kx_0$ can be freely adjusted using the externally applied tension $\tau_{\rm applied}$, or by adjusting the anchoring point of the longitudinal spring x_0. By a suitable choice of x_0, it can be made to vanish. We assume that the filament's ends are pinned to the x axis and torque free: u and $\partial_x^2 u$ vanish at the end points. This choice enables one to expand the transverse undulations in a sine expansion

$$u(x,t) = \sum_p u_p(t)\sin(px), \tag{3}$$

with wave numbers

$$p_n = n\pi/\ell, \tag{4}$$

where $n = 1, 2, \ldots$.

This Hamiltonian provides minimal coupling of a filament in a network to its surroundings (treated as a linear elastic solid). It is necessarily nonlinear. The assumption of instantaneous tension propagation will eventually be violated at sufficiently high wave number since these undulatory modes will relax faster than the tension propagation time. Accounting for tension propagation introduces other nonlinearities to the Hamiltonian, which have been extensively studied [27–29]. We return to the relation of our paper to these studies in Sec. IV A.

The network is overdamped, being immersed in a viscous fluid with viscosity η so that inertial effects may be ignored. We treat the hydrodynamic forces on the filament using resistive-force theory, where the drag force is linear in velocity and decomposes locally into a component perpendicular to (with coefficient $\xi_\perp$) and parallel to (with coefficient $\xi_\parallel$) the mean tangent $\hat{t} \approx \hat{x}$. In terms of the position vector of a segment of the filament, $\vec{u} = (x, u_1(x), u_2(x))$, where the 1 and 2 subscripts label the coordinates transverse to the direction of the undeformed filament $\hat{x}$ and the drag force is [30]

$$[\xi_\parallel \hat{t}\hat{t} + \xi_\perp(\mathbb{1} - \hat{t}\hat{t})]\cdot\partial_t\vec{u} = -\vec{F}_{\rm drag}, \tag{5}$$

where the drag coefficients are given by $\xi_\perp \approx \frac{4\pi\eta}{\ln \ell/a}$ and $\xi_\parallel \approx \xi_\perp/2$. We neglect any modification of the effective drag per unit length near the filament's ends, and we neglect any nonlocal hydrodynamics which produce logarithmic time corrections [10,31]. The drag terms retained give the leading contribution to the drag forces in slender body theory, which provides a power series in $\ln(\ell/a)^{-1}$ [32] at zero Reynolds number. Lastly, if we keep the drag forces acting on the filament only to linear order in u, we may neglect the drag associated with tangential motion.

We now obtain overdamped, model A dynamics [33]:

$$\xi_\perp\partial_t u(x,t) = -\delta H/\delta u(x,t) + \zeta(x,t). \tag{6}$$

We also include Gaussian white noise

$$\langle\zeta(x,t)\zeta(x',t')\rangle = 2\xi_\perp k_BT\delta(x-x')\delta(t-t') \tag{7}$$

in the stochastic equation of motion, Eq. (6), consistent with the fluctuation-dissipation theorem. The analysis presented here is immediately generalizable to nonequilibrium and frequency-dependent noise, as long as it remains Gaussian.

B. Spring-free results

We first review the previously studied dynamics of a filament with fixed applied tension and no coupling to springs. The Langevin equation is linear and admits a normal mode decomposition in terms of half integer wavelength sine waves discussed above. Integrating over frequencies and averaging

with respect to the white noise produces the dynamic correlation function for the amplitudes of these sine waves [2] [see Eqs. (3) and (4)]:

$$\langle u_p(t)u_p(0)\rangle = \frac{2k_BT}{\ell}\frac{e^{-\gamma_p^0 t/\xi_\perp}}{\gamma_p^0}, \tag{8}$$

where we have introduced

$$\gamma_p^0 = \kappa p^4 + \tau p^2, \tag{9}$$

so that $\gamma_p^0/\xi_\perp$ is the wave-number-dependent decay rate. There are no cross correlations between amplitudes of different normal modes.

There is a crossover between tension- and bending-dominated relaxational dynamics, set by the *tension length*:

$$\ell_\tau = \sqrt{\kappa/\tau}. \tag{10}$$

In the long-wavelength $\lambda \gg \ell_t$ tension-dominated regime, modes have an approximate relaxation time $\tau_{\rm relax} \sim \frac{\eta\lambda^2}{\tau\ln(\ell/a)}$. In the short-wavelength bending-dominated regime, modes have an approximate relaxation time $\tau_{\rm relax} \sim \frac{\eta\lambda^4}{\kappa\ln(\ell/a)}$. With vanishing applied tension, one observes a very broad range of relaxation times due to the λ^4 dependence. We now consider dynamics with the inclusion of the longitudinal spring, which mixes the filament's normal modes.

III. THE LONGITUDINAL SPRING: PERTURBATIVE EXPANSION

We hereafter work in units such that $k_BT = 1$. At the end of any calculation, we must then input factors of k_BT where units of energy are needed. In these units, we can use the Einstein relation

$$D = \xi_\perp^{-1} \tag{11}$$

to freely switch from $\xi_\perp$ to D, the latter of which represents a diffusion constant times a length. We now return to the full model A equation of motion defined by Eq. (6). By using Eqs. (1) and (2), we find

$$\frac{\partial u_p}{\partial t} = -D\gamma_p^0 u_p - Dk\Delta\ell u_p + h_p + \zeta_p, \tag{12}$$

where $\zeta_p(t)$ and $h_p(t)$ represent noise and externally applied transverse force, respectively, each absorbing a factor of D. From Eq. (7), we infer that equilibrium correlations of the Gaussian white noise obey the usual relation

$$\langle\zeta_p(t)\zeta_{p'}(t')\rangle = (4D/\ell)\delta_{pp'}\delta(t-t'). \tag{13}$$

The second term on the right hand side of Eq. (12), proportional to k, couples each mode (labeled by p) to changes in the total projected length of the filament, which depends on a sum over the square of amplitudes of all the dynamical modes. As a result, this term in the equation of motion is nonlinear. In order to systematically compute correlation functions in the presence of this nonlinearity, we make use of the MSRJD functional integral method [25,34].

We start by introducing the moment generating MSRJD functional

$$Z[j,\bar{j}] = \int \mathcal{D}[i\bar{u}(x)]\mathcal{D}[u(x)]e^{-\int(\mathcal{A}(\bar{u},u)-\bar{j}\bar{u}-ju)dxdt}, \tag{14}$$

with the action $\mathcal{A}$ separated into a Gaussian part $\mathcal{A}_0$, the nonlinear and spring-dependent correction $\mathcal{A}_{\rm int}$, and a term representing the external h-dependent forcing:

$$\mathcal{A}[u(x,t),\bar{u}(x,t)] = \mathcal{A}_0 + \mathcal{A}_{\rm int} + D\int dxdt\,\bar{u}h. \tag{15}$$

The Gaussian part is

$$\mathcal{A}_0 = \int dtdx\{\bar{u}[\partial_t + D(\kappa\partial_x^4 - \tau\partial_x^2)]u - D\bar{u}^2\}, \tag{16}$$

and the nonlinear interaction is

$$\mathcal{A}_{\rm int} = -\frac{Dk}{2}\int dtdxdy\,\bar{u}(x,t)\frac{\partial^2 u(x,t)}{\partial x^2}\left(\frac{\partial u(y,t)}{\partial y}\right)^2. \tag{17}$$

For the nonlinear action, we have explicitly written out the spatial and time dependencies. Each field is evaluated at the same time (a consequence of instantaneous tension propagation), yet there are two independent spatial variables x and y (nonlocality).

Finally, we recall that $(n,\bar{n})$-point cumulants, representing response functions and correlation functions, are computed via functional derivatives of the logarithm of the MSRJD functional:

$$\left\langle\prod_{i,k}^{n,\bar{n}} u_i\bar{u}_k\right\rangle = \prod_{i,j}^{n,\bar{n}}\frac{\delta}{\delta j_i}\frac{\delta}{\delta\bar{j}_k}\ln Z[j,\bar{j}]|_{j=\bar{j}=0}, \tag{18}$$

where the brackets denote averages over the stochastic forces $\zeta(x,t)$. Specifically, by taking a derivative $\delta\langle u(x,t)\rangle/\delta h(x',t')|_{h(x',t')=0}$, we obtain the transverse linear response function:

$$\chi_{uu}(x,x';t,t') = D\langle u(x,t)\bar{u}(x',t')\rangle. \tag{19}$$

The source field $\bar{j}$ provides the same information as h. Hereafter we set $h = 0$. The response function is trivially related to the propagator $G(x,x';t,t')$ of the theory via a factor of D:

$$G(x,x';t,t') = D^{-1}\chi_{uu}(x,x';t,t'). \tag{20}$$

We also define the dynamic or time-dependent correlation function

$$C(x,x';t,t') = \langle u(x,t)u(x',t')\rangle, \tag{21}$$

hereafter referred to as the *correlator*. Given knowledge of $\chi_{uu}(x,x';t,t')$, it can be found easily via the fluctuation-dissipation theorem, so it need not be calculated independently, at least for the equilibrium dynamics that we study here.

We have chosen the Ito formulation of the Langevin equation, such that the Jacobian of our field transformation from $\zeta(x,t)$ to $u(x,t)$ is unity. This corresponds to the step

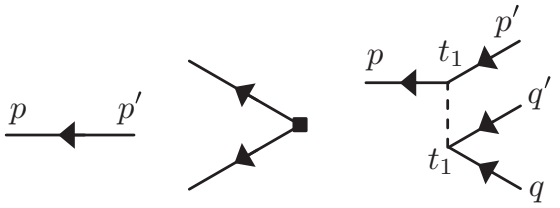

FIG. 2. Diagrams contributing to the perturbation theory of the $(u, \bar{u})$ fields. The propagator (left) is a function of a single p and the time difference: $\langle u_p(t)u_{p'}(t')\rangle = \delta_{pp'}G^0_p(t-t')$. The noise vertex (middle) produces two outgoing lines, and has a coefficient D. The interaction vertex (right) is equivalent to $\frac{-Dk\ell^2}{8}p^2q^2\delta_{pp'}\delta_{qq'}$. It carries two Kronecker deltas, and depends on two wave numbers p and q. This is a consequence of the spatial nonlocality of the nonlinear interaction. Dashed lines connect two points at equal times. In the interaction vertex (right), we associated a factor of $p^2\delta_{pp'}$ $(q^2\delta_{qq'})$ with each vertex of the dashed and solid lines, and a factor of $\frac{-Dk\ell^2}{8}$ with the dashed line itself.

function continuation $\Theta(0) = 0$, and, as a result, all perturbative terms consisting of closed response loops evaluate to zero, consistent with causality. For general time ordering schemes, closed response loops can be shown to be canceled by the appropriate Jacobian factor, ensuring that the physical result is independent of discretization choice [25].

Equations (14) and (15) enable the full machinery of diagrammatic perturbation theory in k. Expectation values with respect to the Gaussian action are denoted by the brackets $\langle\ldots\rangle_0$. The diagrammatic rules are summarized in Fig. 2. In wave-number space, the Gaussian propagator is proportional to a Kronecker delta $\delta_{pp'}$, and therefore depends only on a single wave number. The retarded $(+)$ and advanced $(-)$ propagators are given by

$$G^{0,\pm}_p(t) = \frac{2}{\ell}\theta(\pm t)e^{\mp\gamma^0_p t}, \tag{22}$$

and represented by a directed line from earlier to later times. The comma in the superscript emphasizes that the zero is a label, and not related to whether the propagator is advanced or retarded. The step function allows us to identify outgoing lines as $\bar{u}$ fields and incoming lines as u fields.

One may further define an undirected line to be the bare correlator

$$C^0(x, y, t) = \langle u(x, t)u(y, 0)\rangle_0. \tag{23}$$

However, since the bare correlator is related to the transverse linear response function via the fluctuation-dissipation theorem, we can avoiding introducing the additional undirected propagator by treating the noise term $\approx D\bar{u}^2$ in Eq. (16) as a new vertex [25] denoted by the filled square in the middle of Fig. 2.

The spring-induced nonlinearity generates a spatially nonlocal but instantaneous vertex. As a result, the bare vertex shown in Fig. 2 carries two independent Kronecker deltas in wave number and a delta function in time (dashed line), as well as four factors of wave number. See the caption of Fig. 2 for further details. We can easily switch from the time

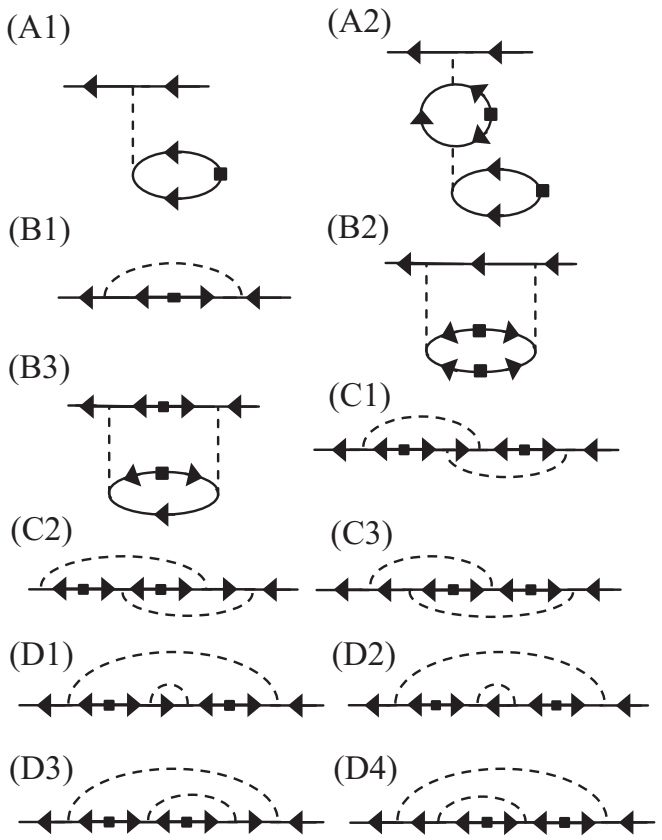

FIG. 3. All diagrams contributing to the self-energy [see definition preceding Eq. (25)] through $\mathcal{O}(k^2)$. There are two $\mathcal{O}(k)$ contributions, A1 and B1. Diagram labels containing an A and a B represent contributions to tension and spring constant renormalization, respectively. For detailed calculations, see Appendix A. Diagrams A1 and B1 are later used to renormalize tension [Eq. (34)] and self-consistently compute the self-energy [Eq. (28)].

domain to the frequency domain, by Fourier transforming the fields,

$$u_p(t) = \int_{-\infty}^{\infty}\frac{d\omega}{2\pi}u_p(\omega)e^{-i\omega t}, \tag{24}$$

and imposing frequency conservation at each vertex.

Using these diagrammatic rules, we compute the k-dependent corrections to the propagator to two-loop order, which is also second order in k. Generally, in perturbation theory these corrections can be neatly grouped into a self-energy $\Sigma_p(\omega)$, defined by the relation $\langle G_p(\omega)\rangle^{-1} = (G^0_p)^{-1}(\omega) - \Sigma_p(\omega)$ [34]. The physical interpretation of this quantity is found in the shift of the bare decay rate from Eq. (9), so that $\gamma^0_p \to \gamma^0_p - \frac{2}{D\ell}\Sigma_p(\omega)$. As such, we define the adjusted self-energy:

$$\tilde{\Sigma}_p(\omega) = \frac{2}{D\ell}\Sigma_p(\omega), \tag{25}$$

which is precisely the shift in γ^0_p.

All the necessary diagrams for this calculation are shown in Fig. 3, and we refer to them hereafter by their label in

that figure, beginning with A1 at the top and continuing to D4 in the bottom right. They are individually calculated in Appendix A. Here, we report the full two-loop self-energy (writing out k_BT explicitly for clarity):

$$\tilde{\Sigma}_{\bar{p}}(\Omega) = -\frac{kk_BT\bar{p}^2}{\kappa}\left[\frac{1}{\bar{p}^2+1} + \frac{1}{2}\sum_{\bar{q}}\frac{1}{\bar{q}^2+1}\right] + \frac{k^2k_B^2T^2}{\kappa\tau^2}\left[\frac{\bar{p}^2}{2(\bar{p}^2+1)^3} + \frac{3\bar{p}^4}{(\bar{p}^2+1)^2[-i\Omega+3\bar{p}^2(\bar{p}^2+1)]}\right.$$
$$\left. + \frac{1}{2}\frac{\bar{p}^2}{(\bar{p}^2+1)}\sum_{\bar{q}}\frac{1}{(\bar{q}^2+1)^2}\left(1-\frac{-i\Omega}{-i\Omega+2\bar{q}^2(\bar{q}^2+1)+\gamma_{\bar{p}}}\right) + \frac{\bar{p}^2}{4}\sum_{\bar{q}}\frac{1}{\bar{q}^2+1}\sum_{\bar{q}}\frac{1}{(\bar{q}^2+1)^2}\right]. \quad (26)$$

We have nondimensionalized the wave numbers and frequencies using a characteristic wave number of the tensed, spring-free system, $\sqrt{\kappa/\tau}$, and its corresponding frequency. This wave number sets the transition between tension-dominated modes (at longer wavelength) and bending-dominated ones (at shorter wavelengths). Thus, we define dimensionless variables $\bar{p} = p\sqrt{\kappa/\tau} = p\ell_\tau$ and frequencies $\Omega = \frac{\omega\kappa}{D\tau^2} = \omega/\omega^*$. These units are convenient, provided that the tension is not so small that $\ell_\tau \approx \ell$, but they are primarily used in order to aid in a qualitative analysis of Eq. (26). For an alternative scheme valid at small τ, see Eq. (A10).

The $\mathcal{O}(k)$ correction is negative, and proportional to $\bar{p}^2$, which tells us that it renormalizes the effective tension to a larger value. This is expected, as the spring stiffens the filament to elongation, causing it to relax faster. To analyze the effects of the spring beyond first order, we categorize the two-loop self-energy into three types of contributions, beginning with the most dominant. The first group consists of type A diagrams in Fig. 3. These are $\approx\bar{p}^2$ so they become appreciable at large wave number. Due to the summations, they also grow with system size, i.e., filament length. As we will see in Sec. IV A (and commented on more in Appendix A), these correspond to a renormalization of the tension, and may be eliminated by using a self-consistent approach to the Green's function.

The second group consists of the type B diagrams in Fig. 3. After τ renormalization, these are the next most important class of diagrams. We will later find that they correspond to renormalization of the spring constant k. At large $\bar{p}$, they plateau to a constant value, and, at small $\bar{p}$, they decay as $\bar{p}^2$. These corrections are important for $\bar{p} \leqslant 1$. These contributions are largest at zero frequency, where they acquire a prefactor $\approx\sum_{\bar{q}}(\bar{q}^2+1)^{-2}$. But this remains small when compared to the type A diagrams, which are proportional to $\sum_{\bar{q}}(\bar{q}^2+1)^{-1}$. In general, we will find (see Sec. IV B) that any diagram containing a solid loop with n outgoing dashed lines will be proportional to a summation $\sum_{\bar{q}}(\bar{q}^2+1)^{-n}$, and thus represent increasingly smaller contributions.

The third and final group consists of both type C and D diagrams of Fig. 3. These diagrams have a single solid line with crossed (type C) or uncrossed (type D) dashed lines. At large $\bar{p}$, these vanish and are therefore small compared to the diagrams of the first (A) and second groups (B). At small $\bar{p}$, they go to zero as $\bar{p}^2$; however, they lack a summation compared to the other terms in Fig. 3 and are thus still smaller. At $\mathcal{O}(k^2)$, these summations are $\approx\sum_{\bar{p}}\bar{p}^{-2}$. As a result, we infer that the missing summations in type C and D diagrams cause them to be about an order of magnitude smaller than the contributions from the other $\mathcal{O}(k^2)$ diagrams. Furthermore, at high frequency, the contributions from the crossed (C) diagrams are smaller than those from noncrossing (D) diagrams. This suggests that we may ignore crossed diagrams in any self-consistent treatment of the dynamics, as described below. This distinction between the crossing and noncrossing diagrams is analogous to impurity scattering in condensed matter, where one also finds that crossing diagrams in electron impurity scattering calculations may be safely ignored [35,36].

We now use the previous analysis to develop a self-consistent approximation for the propagator of Eq. (20) in frequency and wave-number space. The principal effect of the longitudinal spring is to renormalize tension. The details of that process will be shown in Sec. IV A. We account for this by defining

$$\gamma_p = \kappa p^4 + \tau_R p^2, \quad (27)$$

which everywhere replaces γ_p^0. τ_R is the renormalized tension due to the longitudinal spring. We next incorporate the remaining first-order correction (diagram A1), by considering it as the first term in a series of diagrams that contain a single solid line, with no crossed dashed lines [the $\mathcal{O}(k^2)$ term in this series consists of all type D diagrams in Fig. 3]. The infinite summation can quickly be achieved by demanding that the self-energy is equal to the contribution in diagram A1, so long as we replace the bare propagators by dressed ones. This leads to the self-consistent equation

$$\tilde{\Sigma}_p^{\mathrm{NCA}}(\omega) = -\frac{kk_BTp^4}{\gamma_p - \tilde{\Sigma}_p^{\mathrm{NCA}}(\omega)}, \quad (28)$$

known as the noncrossing approximation (NCA). This is certainly correct to $\mathcal{O}(k)$, and as $\omega\to\infty$ becomes precise to all orders in k. Since this is a self-consistent equation, we are free to extend k to large values where we can see its effect. Equation (28) is algebraic, and we easily find the solution:

$$\tilde{\Sigma}_p^{\mathrm{NCA}}(\omega) = \frac{\gamma_p}{2}\left(1-\sqrt{1+\frac{4kk_BTp^4}{\gamma_p^2}}\right). \quad (29)$$

The simplicity of this result is a direct consequence of the spatial nonlocality of our interaction; since dashed lines do not carry wave number, there is no summation over modes in diagram A1. From $\tilde{\Sigma}_p^{\mathrm{NCA}}(\omega)$, we find the NCA transverse linear response function:

$$\chi_p^{\mathrm{NCA}}(\omega) = \frac{2D/\ell}{-i\omega + \frac{1}{2}D\gamma_p\left(1+\sqrt{1+4kk_BTp^4/\gamma_p^2}\right)}. \quad (30)$$

Using the fluctuation-dissipation theorem and reinserting k_BT where necessary to work in physical units, we obtain the dynamic correlator

$$C_p^{\rm NCA}(\omega) = \frac{4k_BT/\xi_\perp \ell}{\omega^2 + \frac{\gamma_p^2}{4\xi_\perp^2}\left(1+\sqrt{1+4k k_BT p^4/\gamma_p^2}\right)^2}. \tag{31}$$

At low tension, we intuitively expect the effect of the longitudinal spring to be stronger. We thus seek units in which the tension can easily be taken to small values. Per the discussion of Sec. II B, at low wave number, the system is in a tension-dominated regime. Accordingly, we switch to a dimensionless length scale by factoring out the wave number of the lowest mode $p_1 = \pi/\ell$. We also adopt a dimensionless tension, spring constant, and frequency:

$$\phi = \frac{\tau \ell^2}{\kappa \pi^2}, \tag{32a}$$

$$\bar{k} = \frac{k k_BT \ell^4}{\kappa^2 \pi^4}, \tag{32b}$$

$$\bar{\omega} = \frac{\omega \xi_\perp \ell^4}{\kappa \pi^4}. \tag{32c}$$

To compute $C_p(\omega)$, we must further calculate tension renormalization. In terms of ϕ, this amounts to the replacement

$$\phi_R = \phi + \Delta\phi, \tag{33}$$

where $\Delta\phi$ is defined by the self-consistent equation

$$\Delta\phi = \frac{\bar{k}}{2}\sum_{n=1}^{\infty}\frac{1}{n^2+\phi+\Delta\phi}. \tag{34}$$

This equation can be derived by approximating the entire self-energy correction by the dominate diagram A2 in Fig. 3, provided we replace the loop propagator with the dressed one. This approximation is discussed more fully in the context of the mean-field theory (MFT) in Sec. IV A. In terms of mode number n, we find the correlator to be

$$C_n^{\rm NCA}(\bar{\omega}) = \frac{4k_BT\xi_\perp \ell^7/\kappa^2\pi^8}{\bar{\omega}^2 + \left[\frac{1}{2}n^2(n^2+\phi_R)\left(1+\sqrt{1+\frac{4\bar{k}}{(n^2+\phi_R)^2}}\right)\right]^2}. \tag{35}$$

In Fig. 4, we plot the NCA correlator as a function of wave number. Generically there are three regimes going from low to high mode number. There is a low wave-number plateau transitioning into an n^{-4} decay, followed by an n^{-8} decay at sufficiently high mode numbers. The effect of the spring is to shift these transitions to lower mode number. For sufficiently high spring constants, the plateau regime may disappear entirely as shown by the (blue and black) solid curves in the figure. The condition for the appearance of the plateau is that $\bar{\omega} > \max\{n^4/4, \phi/4\}$ for some $n \geqslant 1$. The principal effect of the spring is still tension renormalization. Even as $\phi \to 0$, the longitudinal spring ensures that the filament still behaves as if it were under tension. For finite values of the applied tension, the effect of the spring still increases the total effective or renormalized tension, moving the transition to higher-frequency, bending-dominated fluctuations to still higher modes. The fact that the mode where the fluctuations

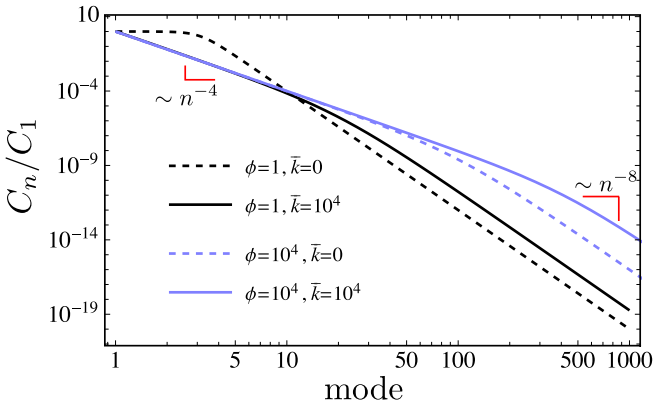

FIG. 4. NCA dynamical correlation function normalized by its first mode at both low (black) and high (blue) tension in the presence (solid) or absence (dashed) of the longitudinal spring. $\bar{\omega} = 100$. The solid black curve overlaps with the solid blue curve at low mode numbers, indicating that the spring generates tension in the absence of any preexisting tension, given in a nondimensionalized form as ϕ. In the presence applied tension $\phi > 0$, the spring increases the effective tension, pushing the transition from tension- to bending-governed fluctuations to higher mode numbers (blue curves).

change from stretching to bending dominated moves in response to the external spring suggests that the effects of even a weak spring will be most easily observed near this tension-to-bending transition ($p = \ell_\tau^{-1}$) of the spring-free model.

In Fig. 5, we look at how varying the applied tension and spring constant shifts the lowest mode $C_1(\omega)$. If the spring does not significantly alter $\Delta\ell$, then the tension $k\Delta\ell$ created by the spring increases linearly in k. However, due to the self-consistent condition, at high k, $\Delta\ell$ diminishes, causing tension to increase as $k^{2/3}$. We discuss this scaling more fully in Sec. IV A. As a result, the correlator decays like $\bar{k}^{-4/3}$, as shown in the top panel of Fig. 5. The transition occurs when $k^* = \tau/\Delta\ell$, which we approximate as $k^* \approx 12\kappa\tau/k_BT\ell^2$ by replacing $\Delta\ell$ with its small tension and spring-free result [26].

We can also see the transition in the correlation function by keeping k constant and varying tension. The correlator transitions from being ϕ independent to decaying as ϕ^{-2} with increasing ϕ, as shown in the bottom panel of Fig. 5. The dependence of the correlator upon applied tension is the same as in the spring-free model. The transition occurs once ϕ is greater than both $4\bar{\omega}^2$ (for the lowest mode) and the renormalized tension $\Delta\phi$, due to the spring. As a result, the spring washes out the effect of small applied tensions, replacing the overall tension with its renormalized value. We now turn to a justification of the approximations outlined above, and derive results concerning projected length fluctuations. Our main tool will be functional techniques using the MSRJD formalism.

IV. PROJECTED LENGTH AUXILIARY FIELD THEORY

The spatially nonlocal theory presented here was previously examined in equilibrium, where the nonlocal aspect allowed for a complete resummation of diagrams contributing to the two-point function [13]. In the dynamical version,

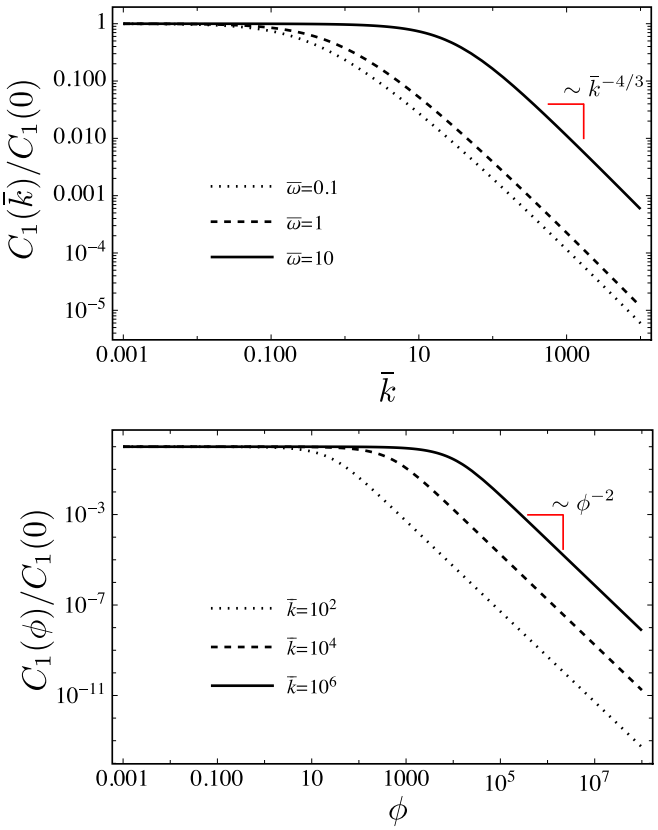

FIG. 5. Lowest mode of the dynamic correlation function vs (top) spring constant and (bottom) applied tension. The top panel is evaluated at low tension, $\phi = 10^{-2}$, and the bottom panel is evaluated at $\bar{\omega} = 1$. At large $\bar{k}$, the effective tension grows sublinearly as $\approx \bar{k}^{2/3}$, leading to the $\bar{k}^{-4/3}$ dependence of C_1. In the bottom panel, the lowest mode dynamic correlation function decays as ϕ^{-2}, which is identical to the spring-free $k = 0$ case. The transition to the ϕ^{-2} decay occurs at tensions higher than $\phi \approx \bar{k}\langle\Delta\ell\rangle$.

however, this resummation fails. The previous calculation of equal-time correlation functions allowed for a great simplification due to the fact that all of these diagrams collapsed into one of two groups (see Ref. [13]). The calculation of dynamical correlations here, however, introduces a time associated with each interaction. This time ordering makes all the previously identical diagrams from Ref. [13] distinct. Since, in the dynamical theory, dashed lines carry frequency, there are an infinite number of inequivalent single-line diagrams, differentiated by the arrangement of dashed-line contractions (for example, compare the class C and D diagrams in Fig. 3).

Despite this complication, we may still proceed along the lines of Ref. [13]. Inspection of Eq. (2) suggests that the Hamiltonian is more naturally expressed in terms of $\Delta\ell(t)$ rather than $u(x,t)$. This will allow us to more easily compute projected length fluctuations $\langle\Delta\ell(t)\Delta\ell(t')\rangle$, which are relevant for experiments measuring the dynamic shear modulus. As a tradeoff, solving for the two-point function, $\langle u_p(\omega)u_{p'}(\omega')\rangle$, will be harder.

In order to change functional integration variables from $u(x,t) \to \Delta\ell(t)$, we first employ a Hubbard-Stratonovich transformation to write the quartic interaction, $\frac{1}{2}k\Delta\ell^2$, in

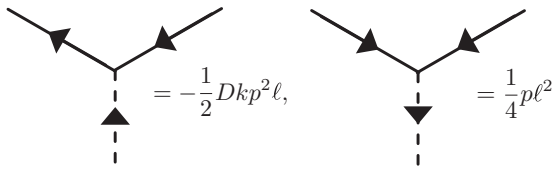

FIG. 6. $\lambda\bar{u}u$ and $\bar{\lambda}uu$ interactions. The Hubbard-Stratonovich transformation cuts the four-point vertex into two three-point vertices. Dashed lines are now directed, with λ incoming and $\bar{\lambda}$ outgoing.

terms of an interaction with auxiliary fields $\lambda$and$\bar{\lambda}$. This amounts to using the identity [37]

$$e^{-\int dt\bar{z}z} = \int \mathcal{D}(\bar{\lambda},\lambda)e^{-\int[\bar{\lambda}\lambda-\bar{z}\lambda-\bar{\lambda}z]dt} \tag{36}$$

in Eq. (14), while making the identifications $\bar{z} = -Dk\int \bar{u}u''dx$ and $z = \Delta\ell = \frac{1}{2}\int u'^2dx$. Diagrammatically, this transformation severs the undirected dashed line into the two three-point vertices depicted in Fig. 6. This transformation is essentially a δ function, acting to assign the change in projected length to the variable $\lambda(t)$. We may alternatively arrive at this step by introducing a Lagrange multiplier into the Hamiltonian, writing down the Langevin equation, then finding the MSRJD functional.

We now add additional source terms $\int dt\, j_\lambda(t)\lambda(t) + \bar{j}_\lambda\bar{\lambda}(t)$ to the expanded functional, which will generate correlations of the auxiliary λ and $\bar{\lambda}$ fields. To understand the physical meaning of these new auxiliary fields, we take the functional derivatives $\frac{\delta}{\delta j_\lambda}$ and $\frac{\delta}{\delta\bar{j}_{\bar{\lambda}}}$ of the generating functional before and after integration over $(\bar{\lambda},\lambda)$, and compare the results. $\delta Z[j_\lambda,\bar{j}_{\bar{\lambda}}]/\delta j_\lambda$ produces the moments of $\Delta\ell(t)$. As a result, there is a one-to-one correspondence between expectation values of $\lambda(t)$ and $\Delta\ell(t)$. That is, for any N-point correlation,

$$\left\langle\prod_i^N \lambda(t_i)\right\rangle = \left\langle\prod_i^N \Delta\ell(t_i)\right\rangle. \tag{37}$$

$\bar{\lambda}$ is related to the linear response of the projected length to an applied tension. For a small change in applied tension $\Delta\tau$, this is defined as

$$\chi_{\Delta\ell}(t,t') = \left.\frac{\delta\Delta\ell(t)}{\delta\Delta\tau(t')}\right|_{\Delta\tau=0}. \tag{38}$$

Equation (36) shows that $\bar{\lambda}$ appears conjugate to $\Delta\ell$, in the same manner as would a time-dependent applied tension. Applying two derivatives $\frac{\delta^2\ln Z}{\delta j_\lambda\delta\bar{j}_{\bar{\lambda}}}|_{j_\lambda=\bar{j}_{\bar{\lambda}}=0}$ before and after integration over auxiliary fields, and then comparing the results, we find the linear response is expressed in terms of the auxiliary fields as

$$\chi_{\Delta\ell}(t,t') = k^{-1}[1 - \langle\lambda(t)\bar{\lambda}(t')\rangle]. \tag{39}$$

As a result of the Hubbard-Stratonovich transformation, the action $\mathcal{A}$ now depends on four fields $\mathcal{A}[\bar{\lambda},\lambda,\bar{u},u]$. It is quadratic in the fields $\bar{u}$ and u, so we may integrate them them

out. Doing so yields the effective action

$$\mathcal{A}[\bar{\lambda}, \lambda, \bar{j}, j] = \int \bar{\lambda}\lambda dt + \frac{1}{2}\mathrm{Tr}\ln \mathbf{G}^{-1} - \frac{1}{2}\int \mathbf{j}^T \mathbf{G}\mathbf{j} dt, \tag{40a}$$

$$\mathbf{G}_p^{-1} = \begin{pmatrix} -2D\mathbb{1} & (G_p^+)^{-1} \\ (G_p^-)^{-1} & -p^2\bar{\lambda}\mathbb{1} \end{pmatrix} \tag{40b}$$

plus λ- and $\bar{\lambda}$-dependent source terms. In the above expressions, the lower case, bold letters stand for the vectors of the fields $\mathbf{u} = (\bar{u}, u)$, $\boldsymbol{\lambda} = (\bar{\lambda}, \lambda)$, and $\mathbf{j} = (\bar{j}, j)$. The trace runs over fields. It also includes a summation over wave numbers p. We have defined the 2×2 block matrix (since its components are operators) $\mathbf{G}^{-1}$ in terms of the advanced and retarded propagators:

$$G_p^{\pm}(t, t') = G_p^{0,\pm}(t) e^{\mp Dkp^2 \int_{t'}^{t} \lambda(t'')dt''}. \tag{41}$$

Since $\mathcal{A}$ retains its dependence on the source terms $\mathbf{j}$, we may still generate correlations of the transverse displacement field via functional differentiation, as defined in Eq. (18). As expected, correlations $\langle \mathbf{uu} \rangle$ depend on expectation values of operator inverses containing stochastic fields $\boldsymbol{\lambda}$. We have traded calculating a simple observable with a complex probability functional for a nonlinear observable with a simple probability functional. Correlations with respect to $\Delta\ell$, on the other hand, are evaluated at $\mathbf{j} = 0$ and are tractable, provided we can simplify the trace log appearing in $\mathcal{A}$.

Since the spring constant k appears only in the combination $\approx Dkp^2\lambda$, we may shift integration variables $\lambda \to \lambda/Dk$, thereby putting all of the k dependence in $\mathcal{A}$ into the first term $\int dt\bar{\lambda}\lambda/Dk$. As $k \to 0$, $\mathcal{A}$ oscillates wildly, indicating that saddle-point evaluation of the functional integral becomes exact. We may then carry out a controlled small k expansion of $\mathcal{A}$ about its saddle-point solution $(\bar{\lambda}_0, \lambda_0)$ plus fluctuations. Incidentally, the saddle-point solution λ_0 is *precisely* the average $\langle \Delta\ell(t) \rangle$, regardless of whether or not k is small.

A. Mean-field theory

We investigate the saddle-point solution corresponding to the effective action Eq. (40a), which becomes exact as $k \to 0$. We denote the saddle-point solutions for the auxiliary fields by λ_0 and $\bar{\lambda}_0$. We will find that the saddle-point solution corresponds to a type of dynamical MFT, and henceforth refer to $\bar{\lambda}_0$ and λ_0 as the mean-field solutions.

The saddle-point equations are

$$\delta\mathcal{A}/\delta\lambda = \delta\mathcal{A}/\delta\bar{\lambda} = 0, \tag{42}$$

evaluated at $\lambda = \lambda_0$ and $\bar{\lambda} = \bar{\lambda}_0$. Functional differentiation of the trace log appearing in $\mathcal{A}$ is carried out in the standard way [34], using $\delta_{\bar{\lambda}}\mathrm{Tr}\ln\mathbf{G}^{-1} = \mathrm{Tr}(\hat{\mathbf{G}}\delta_{\bar{\lambda}}\hat{\mathbf{G}}^{-1})$. As $\bar{\lambda}$ appears only in the (22) component of $\mathbf{G}^{-1}$, functional differentiation yields a matrix with 1 in the (22) component, and zeros elsewhere. Taking the matrix product with $\mathbf{G}$ and performing the trace yields the (22) component of $\mathbf{G}$. We emphasize again that $\mathbf{G}^{-1}$ is really a 2×2 block matrix, with each block representing an operator. Since $\mathbf{G}^{-1}$ is not diagonal in either the time or frequency domains, we cannot trivially invert it. Instead, we determine $\mathbf{G}$ via its defining equation $(\hat{\mathbf{G}}^{-1})_{ik}\hat{\mathbf{G}}_{kj} = \delta_{ij}\delta(t - t')$. This yields the result $G_{22} = (\mathbb{1} - p^2\hat{C}_p\bar{\lambda}_0)^{-1}\hat{C}_p$.

Since $\delta\hat{\mathbf{G}}/\delta\lambda = 0$, the first saddle-point equation is trivially

$$\bar{\lambda}_0(t) = 0. \tag{43}$$

The second saddle-point equation can now be easily found by setting $\bar{\lambda}_0 = 0$. We find the second saddle-point equation:

$$\lambda_0(t) = D\sum_p p^2 \int_{-\infty}^{t} [G_p^+(t, t')]^2 dt', \tag{44}$$

where $G_p^+(t, t')$ was defined in Eq. (41). This depends only on λ_0, and we call it the mean-field condition.

There are two alternative ways to interpret this result, each of which adds to our physical understanding. First, in the context of the $(\bar{u}, u)$ diagrammatic perturbation theory defined by Fig. 2, we can recover the mean-field condition by summing over all one-correlator loop corrections to the propagator. These contributions can be grouped into a mean-field self-energy $\Sigma_p^{\mathrm{MFT}}(t)$. We then demand that $\Sigma_p^{\mathrm{MFT}}(t)$ is equivalent to diagram A1 in Fig. 3, when the loop correlator is replaced by a dressed correlator. Looking for a solution of the form $\tilde{\Sigma}_p^{\mathrm{MFT}}(t) = -\bar{k}p^2\lambda_0$ reproduces the mean-field condition. This observation suggests that the mean-field theory is the leading term in an expansion of $\mathcal{A}[\bar{\lambda}, \lambda]$, determined by the maximal number of dashed lines emanating from a closed, solid line loop. We call a subdiagram with n outgoing dashed lines an *n bubble*. The suggestion turns out to be accurate, and is elaborated on more in Sec. IV B.

Second, we may arrive at Eq. (44) by employing a type of mean-field approximation, in which we make the replacement: $\Delta\ell^2 \to 2\langle\Delta\ell\rangle\Delta\ell$ in the Hamiltonian [see Eq. (2)]. The angled brackets denote averages with respect to the noise. Looking at this replacement more closely, we note that the equilibrium average $\langle \Delta\ell(t) \rangle$ must be a constant in time. Here, however, the averaging is applied with respect only to the noise, and not to the initial configuration of the filament. In that case, the average $\langle \Delta\ell(t) \rangle$ can evolve in time from any particular initial condition. The mean-field theory is capable of describing the relaxation of this variable to its equilibrium value. For example, we can consider a situation where the filament is pulled starting at time $t = 0$.

Returning to our mean-field approximation, the MFT Hamiltonian is now linear. The resulting Langevin equation is also linear, and can be solved for $u_p(t)$ in terms of the noise $\zeta_p(t)$ and $\langle \Delta\ell(t) \rangle$. Imposing the self-consistency condition given by the definition in Eq. (1) of projected length, and identifying $\lambda_0(t) = \langle \Delta\ell(t) \rangle$, we reproduce the mean-field condition Eq. (44). Physically, the mean-field approximation assumes that the normal modes respond only to the change in the averaged projected length, and ignore changes in $\Delta\ell$ due to fluctuations of other normal modes. This approach is actually a mean-field *differential* equation for the function $\lambda_0(t)$. The mean-field theory is neatly summarized as the following Langevin equation:

$$\frac{\partial u_p(t)}{\partial t} = -D\left[\gamma_p^0 + kp^2\lambda_0(t)\right]u_p(t) + \zeta_p(t), \tag{45a}$$

with the condition

$$\lambda_0(t) = \frac{\ell}{4}\sum_p p^2\langle u_p^2(t)\rangle. \tag{45b}$$

Combining these two equations results in the integral equation given by Eq. (44) for $\lambda_0(t)$. When solving the integral equation, it is more convenient to work with the time derivative of $\lambda_0(t)$. Following the notation of Hallatschek *et al.* [27–29], we hereafter refer to Eq. (44) as a partial-integro-differential equation (PIDE). The quantity $k\lambda_0(t)$ acts as a time-dependent tension, the value of which depends self-consistently on the instantaneous conformation of the filament. Our model appears similar to those describing nonlinear tension propagation along inextensible filaments [27–29,38]. This is true for both the ordinary and multiscale perturbation theory [28]. These authors obtain a PIDE similar to ours, where our $\lambda_0(t)$ is analogous to their stored thermal length $\langle \varrho(t) \rangle$. Our analysis differs from the previous work in that the inherent longitudinal compliance of the system is concentrated in the external longitudinal spring, rather than the extensional deformation of the filament. The longitudinal spring responds only to a particular, collective degree of freedom of the system (the end-to-end length). Moreover, the longitudinal spring constant can be changed arbitrarily for a filament with fixed elastic compliance, which provides more freedom for exploration.

When comparing our analysis to the multiscale perturbation theory PIDE, the key distinction is that our $\lambda_0(t)$ does not have spatial dependence. Theories of tension propagation in untensed and tensed filaments [28,38–41] allow for a finite propagation speed of tension, which requires that the longitudinal extension be spatially dependent. One way to consider the validity of our instantaneous tension propagation approximation is to ask which modes of the filament relax slowly on the time scale of that tension propagation. This result depends on the length of the filament segment in question. To do this, we use the results on tension propagation provided in Ref. [28]. Taking as reasonable estimates a 1-μm filament and a 17-μm thermal persistence length (consistent with a 1-μm strand of F-actin), we find that modes with wavelengths longer than $1/17$ of the filament's length relax sufficiently slowly for one to take the approximation of instantaneous tension propagation. This suggests that instantaneous tension propagation is a reasonable approximation for shorter filament segments in a network, where only the lowest deformation modes are typically observable. In the case of longer filaments held in, e.g., an optical trap, the effects of the finite speed of tension propagation are likely to be observable. This presents a potentially interesting extension of the current paper.

In Eq. (53), we show the predicted response function of the end-to-end distance in the presence of prestress. While the projected length fluctuations in the absence of prestress have been studied [9–11], there has not been an explicit discussion of the problem with prestress [42].

We leave details of the evaluation of $\lambda_0(t)$ to Appendix B, and here discuss the results. In the long-time limit, $\lambda_0(t)$ must approach its equilibrium configuration, a constant λ_0. Writing $\lambda_0(t) = Dk\lambda_0$, we find λ_0 obeys the self-consistent equation (restoring k_BT for the moment for ease of comparison)

$$\lambda_0 = \frac{k_BT}{2} \sum_p \frac{1}{\kappa p^2 + \tau + k\lambda_0}, \tag{46}$$

which can be interpreted as a renormalization of the tension $\tau \to \tau + k\langle \Delta\ell \rangle$. In terms of the dimensionless tension ϕ [see Eq. (32a)], this is expressed as the shift $\phi \to \phi + \Delta\phi$, where $\Delta\phi$ satisfies the MFT equation in Eq. (34). The MFT dynamics of a filament attached to a longitudinal spring in equilibrium are thus the same as for a semiflexible filament under tension, provided we renormalize tension.

The time-dependent $\lambda_0(t)$ solution is determined by its initial condition. We consider the case where the filament is initially in equilibrium with the longitudinal spring, and then at $t = 0$ we apply a small additional tension $\delta f(t)$ to an already tensed filament with tension $\tau \gg \delta f(t)$. In Appendix B, we derive the general solution for this situation. We define the change in the projected length from its equilibrium value:

$$\delta\lambda_0(t) = \lambda_0(t) - \lambda_0. \tag{47}$$

At $t = 0$, $\delta\lambda_0(t)$ vanishes, and at $t = \infty$ it must plateau to a constant as the system again reaches a new equilibrium. The Laplace transform $\delta\lambda_0(z)$ obeys the equation

$$\delta\lambda_0(z) = -\frac{\tilde{M}(z)}{1 + k\tilde{M}(z)/z} \delta F(z), \tag{48}$$

where the kernel $\tilde{M}(z)$ is defined in Eq. (B16). The function $\delta F(z)$ is the Laplace transform of the time-integrated applied tension defined in Eq. (B9). The negative sign arises because putting a filament under tension causes it to extend, thereby increasing total projected length, and thus decreasing $\Delta\ell$.

We now examine two cases:

$$\delta f(t) = \begin{cases} \text{oscillating:} & f \sin \omega t \\ \text{constant:} & f \end{cases}, \tag{49}$$

corresponding to oscillatory and constant applied tensions, respectively. These lead to the Laplace-transformed integrated tensions

$$\delta F(z) = \begin{cases} \text{oscillating:} & f(z/\omega)/(z^2 + \omega^2) \\ \text{constant:} & f/z^2 \end{cases}. \tag{50}$$

The Laplace transform of the MFT longitudinal linear response is trivially related to $\delta\lambda_0(z)$:

$$\chi_{\Delta\ell}(z) = \delta\lambda_0(z)/f. \tag{51}$$

The remaining step is to take the inverse Laplace transformation in both cases.

We first discuss the oscillatory solution. In the long-time limit, only residues corresponding to the purely imaginary poles will remain. The only contributing poles are due to $\delta F(z)$, which occur at $z = \pm i\omega$. We can thus substitute $\chi_{\Delta\ell}(z \to -i\omega)$ to obtain the long-time oscillatory solution. An alternative derivation is presented later in Sec. IV B using the MSRJD formalism. Comparing $\tilde{M}(-i\omega)$ with $\Pi^+(\omega)$ [defined later in Eq. (61)], and $\chi_{\Delta\ell}(z)$ with the later MSRJD result in Eq. (39), we observe that the MFT Langevin equation exactly reproduces the more rigorous MSRJD analysis. We thus postulate (but do not prove in this paper) that the MFT Langevin equation is capable of providing the exact correlations $\langle \Delta\ell(t_1) \dots \Delta\ell(t_N) \rangle$ for any product of N $\lambda_0(t)$ fields.

The p summation appearing in the kernel $\tilde{M}(z)$ [Eq. (B16)] can be performed, but is unwieldy. It is easily performed numerically. We use that numerical summation to plot $\delta\langle \Delta\ell \rangle/\delta f$ in Fig. 7. Analytically, we look at the long- and short-time limits, and then comment on the transition between the two.

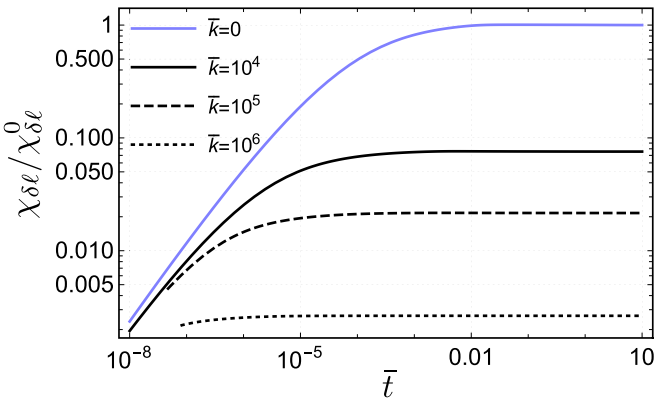

FIG. 7. MFT longitudinal linear response normalized by the plateau value $\chi^0_{\Delta\ell} = \chi_{\Delta\ell}(\bar{t} = \infty, \bar{k} = 0)$ of the spring-free filament. $\bar{t} = t\ell^4\xi_\perp/\kappa\pi^4$. At early times, there is $\bar{t}^{3/4}$ growth, but the function does not exhibit power-law behavior. The longitudinal spring decreases the relaxation time, roughly proportional to $\bar{k}^{4/3}$.

Long and short times correspond to small and large z, respectively. At long times, $\tilde{M}(z \to 0) \sim z$, while at short times $\tilde{M}(z \to \infty) \sim z^{1/4}$. The long-time limit leads to a constant value λ_0, which is determined by the self-consistent Eq. (46) with τ replaced by $\tau + f$.

At short times, z is large, and so the factor of $k\tilde{M}(z)/z \sim z^{-3/4}$ is negligible compared to 1. We find the simpler expression

$$\chi_{\Delta\ell}(z \gg 1) = -\frac{\tilde{M}(z)}{z^2}. \tag{52}$$

The inverse Laplace transform yields

$$\chi_{\Delta\ell}(t \ll 1) = \frac{k_B T}{2} \sum_p \frac{e^{-2Dp^2 t(\kappa p^2+\tau)} - 1}{(\kappa p^2 + \tau)^2}. \tag{53}$$

This is precisely the spring-free result for the longitudinal linear response of a tensed filament.

To extract the short-time behavior, we replace the summation with an integration, extend the limits of integration from zero to ∞, and make the variable substitution $p \to p(2D\kappa t)^{1/4}$. At small t, the p^4 bending terms in the exponent are dominant, leading to

$$\chi_{\Delta\ell}(t \ll 1) \approx \frac{k_B T \ell}{2\pi\kappa^2}(2D\kappa t)^{3/4} \int_0^\infty \frac{e^{-z^4} - 1}{z^4} dz. \tag{54}$$

The integral is $\Gamma(1/4)/3$. From this we find the final result

$$\chi_{\Delta\ell}(t \ll 1) \approx \frac{k_B T \ell \Gamma(1/4)}{3\pi 2^{1/4}\kappa^{5/4}\xi_\perp^{3/4}} t^{3/4}. \tag{55}$$

The short-time power-law growth $t^{3/4}$ is the same as for flexible filaments [2]. However, this is only the leading term at short time. Due to the presence of τ, the filament breaks self-similarity and the function does not obey a power law.

The short-time longitudinal response is bending dominated, and independent of the spring. From Eq. (48), we expect the longitudinal spring to become important when $k\tilde{M}(z)/z > 1$. As $k \to \infty$, the $\tilde{M}(z)/z$ in the numerator and denominator cancel out, leaving the inverse Laplace transform of $-f/zk$, which gives a constant. Thus, the spring shortens the relaxation time. Since, in the short-time limit $\tilde{M}(z) \sim z^{1/4}$, this suggests that the relaxation time to equilibrium decreases with increasing spring constant like $k^{-4/3}$.

In Fig. 7, we plot the response function by performing a numerical inverse Laplace transform of Eq. (51) using Eq. (B17), for several values of k. It exhibits the predicted $t^{3/4}$ spring-free growth. Increasing k shortens the equilibration time.

To conclude the section, we consider how the decay rates of normal modes are altered in the MFT. From Eq. (B2), specifying $u_p(0)$ and then averaging over the noise suggests that normal modes obey a time-dependent decay rate, τ_{decay}, given by

$$\tau^{-1}_{\text{decay}}(t) = \xi_\perp^{-1}\left[\kappa p^4 + \tau p^2 + kt^{-1}\int_0^t \lambda_0(t')dt'\right]. \tag{56}$$

At short times, $\lambda_0(t) \sim t^{3/4}$, which implies an additional stretched exponential prefactor $\langle u_p(t)\rangle \sim e^{-kt^{7/4}/\xi_\perp}$ [again, the average is over noise and $u_p(0)$ is specified]. Since at small times $t > t^{7/4}$, we expect this effect to be difficult to observe in experiment.

B. Fluctuations and random phase approximation

The saddle-point approximation, while accurately calculating $\langle\Delta\ell(t)\rangle$, does not address multipoint correlations of $\Delta\ell(t)$. This prevents us from understanding how the spring-induced nonlinearity affects dynamic fluctuations of $\Delta\ell(t)$. We define the longitudinal correlator

$$C_{\delta\ell}(t,t') = \langle\Delta\ell(t)\Delta\ell(t')\rangle - \langle\Delta\ell(t)\rangle\langle\Delta\ell(t')\rangle \tag{57}$$

to be the correlation functions of the end-to-end distance. This quantity is related to the dynamic shear modulus [8,9] and informs frequency-dependent activity microscopy [12,13].

We account for fluctuations by expanding the trace-log term $\text{Tr}\ln\mathbf{G}^{-1}(\lambda_0 + \delta\lambda, \delta\bar{\lambda})$ of the action [Eq. (40a)] in powers of $\delta\lambda$ and $\delta\bar{\lambda}$, about the saddle point. In principle, one may carry out the expansion to arbitrary order. We stop at the quadratic terms. This truncation is a valid approximation for stiff filaments, where the equilibrium end-to-end contraction is small compared to contour length.

Since we are considering fluctuations about equilibrium, time-translation invariance allows us to Fourier transform to the frequency domain. In frequency and wave-number space, the propagators and correlators appearing in the expansion refer to the saddle-point and MFT values:

$$\bar{G}^+_p(\omega) = \frac{2/\ell}{-i\omega + Dp^2(\kappa p^2 + \tau + k\lambda_0)}, \tag{58a}$$

$$\bar{C}_p(\omega) = \frac{4D/\ell}{\omega^2 + [Dp^2(\kappa p^2 + \tau + k\lambda_0)]^2}. \tag{58b}$$

In Appendix C, we carry out the trace-log expansion to quadratic order, yielding the Gaussian approximation to the action at the saddle point:

$$\mathcal{A}_{\text{eff}}[\delta\bar{\lambda}, \delta\lambda] = \frac{1}{2}\int \frac{d\omega}{2\pi}\delta\boldsymbol{\lambda}^T_\omega \mathbf{M}^{-1}_\omega \delta\boldsymbol{\lambda}_{-\omega}, \tag{59}$$

where the matrix $\mathbf{M}^{-1}_\omega$ is defined in Eq. (C7). This is our final expression for the effective action $\mathcal{A}_{\text{eff}}$. We are primarily

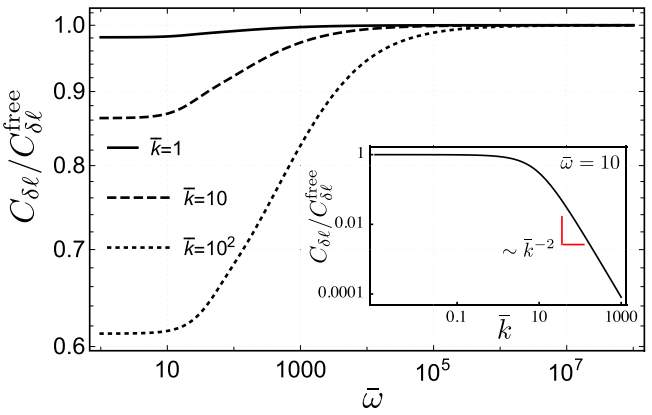

FIG. 8. Ratio of the longitudinal correlator to its spring-free value. $\phi = 1$. At high frequency, individual modes have not relaxed to a new equilibrium that accounts for the longitudinal spring, so the ratio flattens to 1. As frequency decreases, we approach the static result of Eq. (46), whereby we find a reduced amplitude, with zero slope. The inset shows that, for a fixed frequency ($\bar{\omega} = 10$) and zero tension $\phi = 0$, the ratio decays as $\bar{k}^{-2}$ after passing a frequency-dependent crossover spring constant k^*.

concerned with the inverse $\mathbf{M}_\omega$. It is related to fluctuations in the projected length, and its linear response to applied tension. We compute

$$\mathbf{M}_\omega = \begin{pmatrix} 0 & \frac{1}{1+k\Pi^-_\omega} \\ \frac{1}{1+k\Pi^+_\omega} & \frac{\Pi^0_\omega}{|1+k\Pi^+_\omega|^2} \end{pmatrix}, \tag{60}$$

where the polarization functions, $\Pi^\pm_\omega$ and Π^0_ω, are defined as

$$\Pi^\pm(\omega) = \sum_p \frac{Dp^4}{\gamma_p(\mp i\omega + 2D\gamma_p)}, \tag{61}$$

$$\Pi^0(\omega) = \sum_p \frac{2Dp^4}{\gamma_p\left(\omega^2 + 4D^2\gamma_p^2\right)}. \tag{62}$$

The Π^0 function is precisely the Fourier transform of the spring-free correlator [9]. The $\pm$ functions are complex conjugates of one another, i.e., $\Pi^+ = (\Pi^-)^*$. They can be related to Π^0 via a fluctuation-dissipation-like relation [Eq. (C8)]. Using Eq. (39), we relate the Π^+ function to the longitudinal linear response via

$$\chi_{\Delta\ell}(\omega) = \frac{\Pi^+(\omega)}{1 + k\Pi^+(\omega)}. \tag{63}$$

Comparison of the correlation function with $\chi_{\Delta\ell}$ confirms that the fluctuation-dissipation theorem is satisfied.

The ratio

$$\frac{C_{\delta\ell}(\omega)}{C^{\rm free}_{\delta\ell}(\omega)} = \frac{1}{|1 + k\Pi^+(\omega)|^2}, \tag{64}$$

of projected length fluctuations in the presence or absence of a longitudinal spring, makes the effect of the spring more transparent. That ratio is plotted in Fig. 8. We first analyze the k dependence of the ratio. If we slowly increase k, we see that, below $|k\Pi^+(\omega)| = 1$, there is little deviation from the spring-free result. When k is large enough to exceed the bound $|k\Pi^+(\omega)| = 1$, then the end-to-end fluctuations diminish as k^{-2}. This is supported numerically (see the inset of Fig. 8).

It is interesting that below a certain frequency the effect of the longitudinal spring on the end-to-end distance fluctuations is *screened in time*. To make the connection with screening more concrete, consider the low-frequency limit of $\Pi^+(\omega) \sim i\omega$, and then inverse Fourier transform Eq. (64). We obtain an exponential decay (in time) for the ratio of the spring-connected filament end-to-end fluctuations to those of the spring-free case. This screening effect shows that the longitudinal spring changes the filament's dynamics in a way that cannot be simply captured by tension renormalization. This new complexity arises because the filament lengths, stored in the various normal modes, interact through the spring.

The value k^* beyond which screening breaks down is, itself, frequency dependent. Specifically, $k^* \approx |\Pi^+(\omega)|^{-1}$. Since $\Pi^+(\omega)$ is decreasing with ω, screening breaks down at smaller values k^* as ω decreases, bottoming out in the static limit ($\omega = 0$) with a minimum value $\bar{k}^*_{\rm min} = [\sum_{n=1}^\infty (n^2+\phi)^{-2}]^{-1}$. Below this spring constant $\bar{k}^*_{\rm min}$, screening occurs at all frequencies.

The frequency dependence of the ratio of the correlators with and without the spring can be understood similarly. At $\omega = 0$, if $k > k^*_{\rm min}$, then the longitudinal spring shifts the longitudinal correlator to its mean-field result. In the opposite limit where $\omega \to \infty$, screening becomes perfectly effective, and there is no deviation from the spring-free result. In the main panel of Fig. 8, we see that the longitudinal correlator transitions from the spring-dominant, mean-field result to the spring-free result across a range of frequencies that increases with k.

By examining the saddle-point analysis, we obtain further insight into which of the perturbative corrections we have taken into account in this approach. Examining the action in Eq. (59), we claim that it is a renormalization of the dashed line propagators of the original $(\bar{u}, u)$ theory. Since all dashed-line renormalizations are necessarily bubble type diagrams, $\mathbf{M}$ contains the contributions from all two-bubbles (the general n-bubble subdiagram is a solid line loop with exactly n outgoing dashed lines). Taking higher-order terms in the expansion of the trace log will result in bubbles with $n > 2$ external dashed lines, which are exactly the n-bubbles. The fluctuation expansion is not just a k expansion, but a systematic inclusion of higher number bubbles.

We can estimate the relative importance of successive terms. The one-bubble returns just the static change in projected length $\Delta\ell_0$. The two-bubble, $\approx \sum_p G_p^2(\omega = 0) \sim \partial_\tau \langle \Delta\ell_0 \rangle$, is proportional to the static susceptibility $\chi_{\Delta\ell}$, with each higher order gaining another derivative of the projected length with respect to ∂_τ. Since each derivative lowers the summand by p^{-2}, successive terms quickly become small.

Classifying the diagrams in Fig. 3 of the perturbation series, to $\mathcal{O}(k^2)$ they can be divided into one-bubbles, two-bubbles, and the rest. Per the saddle-point analysis, the one- and two-bubbles are the leading and subleading terms, corresponding to renormalization of the effective tension and spring constant. This is consistent with our analysis in Sec. III, where our grouping of diagrams into dominant and subdominant classes was in fact a grouping into n-bubbles.

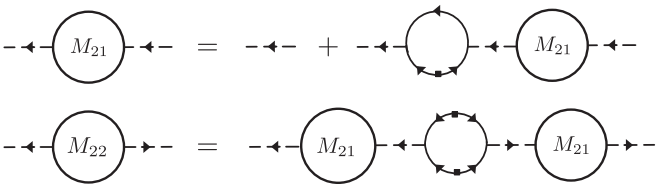

FIG. 9. Random phase approximation for computing the renormalized interaction vertex. When used in a diagram, the directed dashed lines must join to external solid lines according to Fig. 6. M_{ij} refers to the matrix elements of $\mathbf{M}$. $M_{21} = \langle \lambda \bar{\lambda} \rangle$ is directed from a vertex with two incoming lines, to one with an incoming and an outgoing line.

Returning to our analysis of the effective action, we observe that the resummation of bubble diagrams is an approximation known as the RPA [34]. The RPA applies only to the dashed line, which in any actual diagram must be attached to two solid lines according to the rules in Fig. 6. The two-bubble renormalized vertex is given by the diagrams in Fig. 9, which yield the equations

$$M_{21}(\omega) = 1 - \frac{kD\ell^2}{4} \sum_p \int \frac{d\omega'}{2\pi} p^4 \bar{C}_p(\omega' - \omega) \bar{G}_p^+(\omega'), \tag{65a}$$

$$M_{22}(\omega) = |M_{21}(\omega)|^2 \sum_p \int \frac{d\omega'}{2\pi} \frac{p^4\ell^2}{4} \bar{C}_p(\omega - \omega') \bar{C}_p(\omega'). \tag{65b}$$

Solving these reproduces Eq. (60), thus confirming our claim. Since the dashed lines appear only in combination with k, the RPA amounts to a renormalization of k.M_{21} and M_{22} represent effective vertices, the lowest-order terms of which reproduce diagrams B1 and B2 and diagram B3, respectively in Fig. 3.

Finally, we consider the longitudinal response function given in Eq. (63). This provides an estimate for the high-frequency behavior of the dynamic shear modulus of semiflexible networks [40,41], via the relation $\tilde{G}(\omega) = \frac{1}{15}\rho\ell\chi_\omega^{-1} - i\omega\eta$ [9], where ρ denotes the density of filaments. Note that the dynamic shear modulus, $\tilde{G}(\omega)$, must be distinguished from our earlier definitions of propagators. Ignoring the viscous term, in Fig. 10 we plot both $J(\omega)$ and $\tilde{G}(\omega)$ for both $\bar{k} = 0$ and 10^4. $\tilde{G}(\omega)$ possesses three distinct scaling regimes, regardless of the longitudinal spring: a low-frequency regime $\approx\omega$, an intermediate-frequency regime $\approx\omega^{1/2}$, and a high-frequency bending regime $\approx\omega^{3/4}$. The spring does not affect this scaling, but shifts the transition region to higher ω as k increases, which is consistent with our assertion that tension renormalization is the spring's main effect.

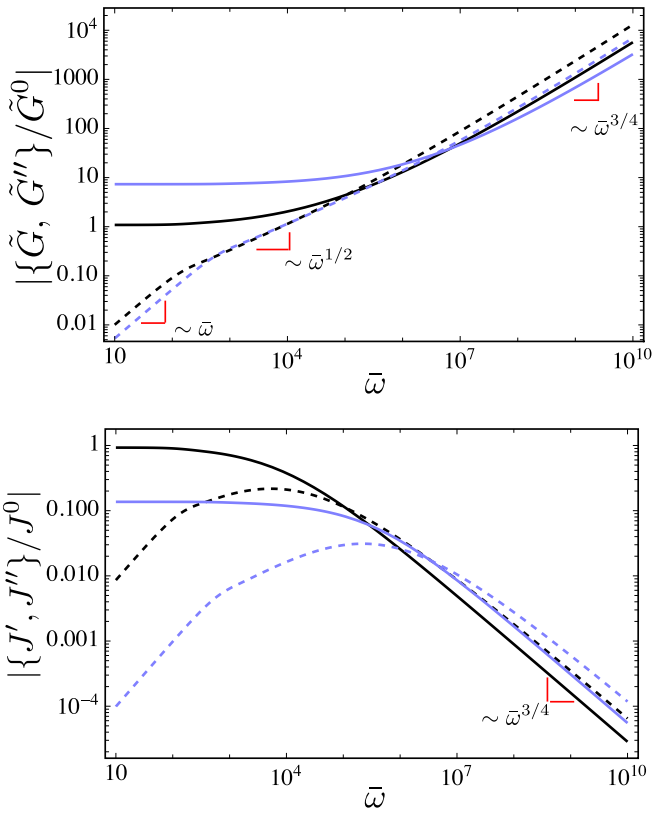

FIG. 10. Real (solid lines) and imaginary (dashed lines) parts of the shear modulus $\tilde{G}(\omega)$ and network compliance $J(\omega)$ for $\bar{k} = 0$ (black) and for $\bar{k} = 10^4$ (blue). $\phi = 10^2$. $\tilde{G}$ and J are normalized by their spring-free plateau values. The transition of $\tilde{G}(\omega)$ from $\omega^{1/2}$ to $\omega^{3/4}$ scaling signals the shift from tension- to bending-dominated behavior [10,38]. The longitudinal spring does not alter the power-law dependence, but shifts the crossover between them to higher frequencies.

V. CONCLUSION

We have extended the static analysis of Ref. [13] to include the dynamics of the fluctuations of a filament in a network, the linear compliance of which is modeled as a Hookean spring attached to the boundary. The principal motive behind these calculations is to provide a precise prediction for the dynamical fluctuations of filaments based on κ, τ, and k, that can then be used to perform local activity microscopy.

The addition of the spring boundary condition introduces a nonlinearity into the problem, which is peculiar in the sense that it is nonlocal in space but local in time. It depends at each instant on the projected length of the whole filament. The peculiarity stems from our assumption of instantaneous tension propagation. The strength of the nonlinearity can be externally governed via the spring constant k.

For a filament bound to a larger network, the spring constant k approximates the compliance of the entire surrounding network. To get an estimate for experimentally relevant values of parameters, we use as an example an F-actin network with shear modulus $G \approx 100$ Pa, and mesh spacing $\xi \approx 0.5$ μm, which we assume is comparable to the mean distance between consecutive cross links along the same filament. Using the relation $G \sim k/\xi$ [26], we estimate a spring constant of 0.05 pN/nm [13]. We further assume a persistence length $\ell_p = \kappa/k_BT$ that is approximately an order of magnitude greater than the filament segment length, and $k_BT \approx 4$ pN nm. These suggest $\bar{k} \sim 10^3$. In these dimensionless units, a tension of 1 pN corresponds to $\phi \sim 10^2$.

The most direct and quantitatively precise experimental test of this analysis is directly examining the dynamics of a single filament tethered to a bead in an optical (or magnetic)

trap. In that case, one can independently control both the mean tension in the filament and the effective spring constant k by varying the position of the optical trap and its intensity, respectively. In this setup, one may imagine two distinct types of measurements. One could observe the end-to-end length fluctuations by tracking the bead in the trap with high spatial and temporal resolution. Or, one could observe the undulations of the filament directly, which would allow one to measure the u correlation functions computed here. In both of these cases, one might also measure the response functions by observing the response of either u or the end-to-end distance of the filament to changes in the trap's center.

We find the main effect of the spring is to renormalize tension. Even for untensed filaments, once a spring is added, the filament behaves as if it were under tension $\tau_R \approx k\langle\Delta\ell\rangle_0$. Perhaps, this blending of spring effects into an effective tension explains the success of previous theories, which have neglected nonlinearities introduced by a longitudinal boundary spring [2,26]. We have shown that an increasing spring constant decreases the relaxation times of all the fluctuating degrees of freedom of the filament. Given a fixed external tension τ, there is a scale $k^* \approx 12\,\kappa\tau/k_BT\ell^2$ of the external spring constant, above which the dominant contribution to tension comes from the spring and not the bare applied tension. Using this crossover, we estimate the minimum spring constant the effect of which on filament dynamics should be observable. For typical filaments on the order of microns (with persistence lengths greater than their contour length) and tensions $\approx$10 pN, we expect this transition to occur at $k \approx 1$(pN/nm). This is achievable near the upper limit of optical trap strength ($\approx$100 pN/100 nm), or by alternatively using a magnetic trap that can achieve higher k values. Optical traps also induce a (weaker) transverse spring at the filament's end point since the beads in the trap are harmonically constrained to the focal plane [43]. This additional constraint on the filament's end points can be handled by switching from the sinusoidal normal modes used here to the ones appropriate for a transverse force-balance condition on the filament's end points (see Ref. [13] and the discussion in Appendix D). A full calculation of the dynamics in this configuration remains to be done.

One could alternatively use optical tweezers to exert localized forces within a network of filaments, putting some of them under tension τ. We predict that increasing τ will not affect fluctuations up until a transition tension $\tau^* \approx kk_BT\ell^2/12\kappa$, after which the amplitude of fluctuations will decrease as τ^{-2}. In the absence of the network compliance (the spring in our model), the transition occurs at a lower tension, which is frequency dependent. One may also look for nontrivial changes in filament tension and fluctuations as a function of network stiffness. Since the change in tension due to the spring is $\Delta\tau \sim k\Delta\ell$, for sufficiently stiff networks where the effective spring constant $k > k^*$, the change in tension switches from a linear k dependence to a weaker one $\approx k^{2/3}$, due to the shortening of $\Delta\ell$. This leads to a $k^{-4/3}$ decrease in the amplitude of transverse fluctuations.

We also considered fluctuations of the end-to-end projected length of the filament, and its response to an applied tension. We found that including the external longitudinal spring does not affect the short-time longitudinal, linear response of projected length to an abrupt change in applied tension. The change in projected length grows initially like $t^{3/4}$, but does not exhibit a power law at longer times. The longitudinal spring, does, however, shorten the relaxation time of the end-to-end length by a factor $\approx k^{-4/3}$. From the response function of the end-to-end distance of a single filament to oscillatory forcing, we can predict the collective dynamic shear modulus of the network using now standard arguments. We find that the spring shifts the transition from tension dominated, $G(\omega) \sim \omega^{1/2}$, to bending dominated, $G(\omega) \sim \omega^{3/4}$, to higher frequencies.

Finally, there is an additional frequency-dependent effect that can be observed from fluctuations in the end-to-end projected length, which arises as a result of the nonlinear interaction the spring induces on normal modes. In the static, $\omega \to 0$ limit, the amplitude of end-to-end fluctuations will be lower than that for a filament not attached to a longitudinal boundary spring. As frequency increases, however, the effect of the spring diminishes, approaching the spring-free result as $\omega \to \infty$. At high frequencies the normal modes adjust so as to screen the effect of the longitudinal spring. We report a minimum value $\bar{k}^*_{\min}$, below which the longitudinal spring is screened at all frequencies. This occurs when $\bar{k}^*_{\min} = [\sum_n (n^2+\phi)^{-2}]^{-1}$. This minimal spring stiffness necessary for complete screening grows with applied tension as $\approx\tau^{3/2}$.

Future directions for this work include a first-principles calculation of the effective spring constant k representing the network. At least, one may imagine pursuing a type of self-consistent analysis by demanding that the force extension relation of the filament coupled to the spring is identical to those of the network filaments, the collective elasticity of which is represented by that spring. Secondly, one may consider how the transverse undulations of a filament in the network (represented by external springs coupled to the end of that filament) behave in response to nonequilibrium driving, such as would be experienced by the filament in a network driven by endogenous molecular motors.

ACKNOWLEDGMENTS

The authors would like to thank the Botvinick group at University of California Irvine for experiments that motivated the study of this problem. The authors acknowledge partial support from NSF Grant No. DMR-1709785.

APPENDIX A: DIAGRAMMATIC PERTURBATION THEORY TO $\mathcal{O}(k^2)$

We compute the adjusted self-energy given in Eq. (25) to $\mathcal{O}(k^2)$. For readability, in this section we drop the zero superscript, with γ_p referring to γ_p^0. When we refer to diagrams appearing in Fig. 3, we are including not only the diagram, but also its combinatorial factor for contracting the legs. We also include a factor of $(-Dk\ell^2/8)^n/n!$ at $\mathcal{O}(k^n)$. Diagram B1 has combinatorial factor 2, A1 has 1, all C and D diagrams have 2^3, B2 has 2^2, B3 has 2^3, and A2 has 2^2.

We calculate for the $\mathcal{O}(k)$ diagrams:

$$\mathrm{A1} = -\frac{1}{2}kp^2\sum_q \frac{q^2}{\gamma_q} \tag{A1}$$

and

$$\mathrm{B1} = -k\frac{p^4}{\gamma_p}. \tag{A2}$$

For the D diagrams, D1 and D2 vanish due to a closed response loop. D3 and D4 give identical contributions, leading us to write the D contribution as

$$\mathrm{D3} + \mathrm{D4} = \frac{k^2p^8}{\gamma_p^3}. \tag{A3}$$

All three of the C diagrams give the same contribution. Summing these gives

$$\mathrm{C1} + \mathrm{C2} + \mathrm{C3} = k^2\frac{3\mathrm{D}p^8}{\gamma_p^2(-i\omega + 3\mathrm{D}\gamma_p)}. \tag{A4}$$

Lastly, for the B diagrams,

$$\mathrm{B2} = k^2\frac{p^4}{\gamma_p}\sum_q \frac{\mathrm{D}q^4}{\gamma_q(-i\omega + 2\mathrm{D}\gamma_q + \mathrm{D}\gamma_p)} \tag{A5}$$

and

$$\mathrm{B3} = k^2p^4\sum_q \frac{\mathrm{D}q^4}{2\gamma_q^2(-i\omega + 2\mathrm{D}\gamma_q + \mathrm{D}\gamma_p)}. \tag{A6}$$

Taking the sum, we simplify to

$$\mathrm{B2} + \mathrm{B3} = \frac{k^2p^4}{2\gamma_p}\sum_q \frac{q^4}{\gamma_q^2}\left(1 - \frac{-i\omega}{-i\omega + \mathrm{D}(2\gamma_q + \gamma_p)}\right). \tag{A7}$$

The last diagram is

$$\mathrm{A2} = k^2p^2\left(\sum_q \frac{q^2}{2\gamma_q}\right)\left(\sum_q \frac{q^4}{2\gamma_q^2}\right). \tag{A8}$$

The adjusted self-energy is simply the sum of these contributions. Altogether we find

$$\tilde{\Sigma}_p(\omega) = -k\left(\frac{p^4}{\gamma_p} + \frac{p^2}{2}\sum_q \frac{q^2}{\gamma_q}\right) + k^2\left[\frac{p^8}{\gamma_p^2}\left(\frac{1}{\gamma_p} + \frac{3\mathrm{D}}{-i\omega + 3\mathrm{D}\gamma_p}\right) + \frac{p^4}{2\gamma_p}\sum_q \frac{q^4}{\gamma_q^2}\left(1 - \frac{-i\omega}{-i\omega + \mathrm{D}(2\gamma_q + \gamma_p)}\right) + \frac{1}{4}p^2\left(\sum_q \frac{q^2}{\gamma_q}\right)\left(\sum_q \frac{q^4}{\gamma_q^2}\right)\right] + \mathcal{O}(k^3). \tag{A9}$$

We may rewrite this in terms of the dimensionless tension, $\phi = \frac{\tau\ell^2}{\pi^2\kappa}$, and dimensionless frequency, $\bar{\omega} = \omega\ell^4/(D\kappa\pi^4)$, as

$$\tilde{\Sigma}_n(\omega) = -\frac{kk_\mathrm{B}T}{\kappa}\left(\frac{n^2}{n^2+\phi} + \frac{n^2}{2}\sum_m \frac{1}{m^2+\phi}\right) + \frac{k^2\ell^4k_\mathrm{B}^2T^2}{\kappa^3\pi^4}\left[\frac{n^2}{(n^2+\phi)^3} + \frac{3n^4}{-i\bar{\omega} + 3n^2(n^2+\phi)} + \frac{1}{2}\frac{n^2}{n^2+\phi}\sum_m \frac{1}{(m^2+\phi)^2}\left(1 - \frac{-i\bar{\omega}}{-i\bar{\omega} + 2m^2(m^2+\phi) + n^2(n^2+\phi)}\right) + \frac{n^2}{4}\sum_{m,m'}\frac{1}{(m^2+\phi)(m'^2+\phi)^2}\right], \tag{A10}$$

where m, m', and n are positive integers, and we have restored factors of $k_\mathrm{B}T$.

Rewriting $\tilde{\Sigma}_p(\omega)$ in terms of the dimensionless wave number $\bar{p} = p\sqrt{\kappa/\tau}$ instead leads to Eq. (26). We can categorize several of the diagrams in terms of the n-bubble expansion. Diagrams of type A contain one-bubbles, and generate a shift in the effective tension. Diagrams of type B contain two-bubbles, and generate a shift in the effective spring constant k. The remaining diagrams are single line topologies.

APPENDIX B: MEAN-FIELD THEORY SOLUTION IN THE TIME DOMAIN

Our starting point is Eq. (45). We begin by defining the integrated projected length

$$\Lambda(t) = \int^t \lambda_0(t')dt', \tag{B1}$$

as the antiderivative of $\lambda_0(t)$. The differential equations of motion [Eq. (45a)] governing the normal modes can be solved in terms of $\lambda_0(t)$. We find

$$u_p(t) = u_p(0)\tilde{\chi}_p(t,0) + \int_0^t dt'\tilde{\chi}_p(t,t')\zeta_p(t'), \tag{B2}$$

where we defined

$$\tilde{\chi}_q(t,t') = e^{-D(\kappa q^4 + \tau q^2)(t-t') - Dkq^2[\Lambda(t) - \Lambda(t')]}, \tag{B3}$$

in agreement with the notation of Refs. [40,41]. The initial condition $u_p(0)$ may either be specified or treated as a random variable. Using Eq. (45b), we can eliminate the normal modes in favor of a single PIDE governing $\lambda_0(t)$. We obtain

$$\frac{d\Lambda}{dt} = \frac{\ell}{4}\sum_q q^2\left\{\chi_q^2(t,0)\langle u_q^2(0)\rangle + \frac{4\mathrm{D}}{\ell}\int_0^t \chi_q^2(t,t')dt'\right\}. \tag{B4}$$

The brackets around $u_p(0)$ indicate an average over these initial amplitudes. Since the average over the initial amplitudes $\langle u_q^2\rangle$ may be taken with respect to any ensemble, this equation can describe the relaxation of a nonequilibrium state. In this

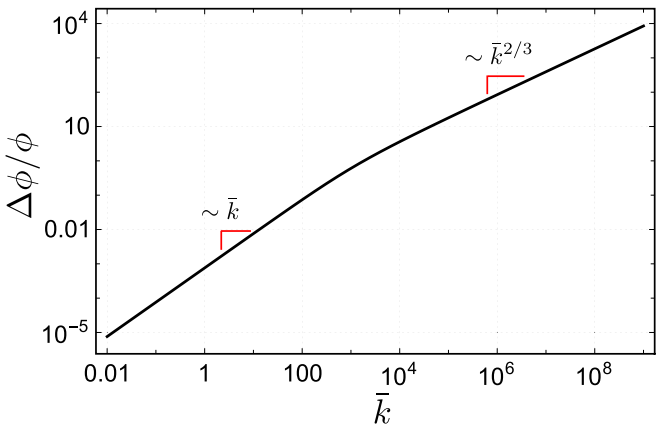

FIG. 11. Growth of additive tension renormalization $\Delta\phi$ as a function of the dimensionless spring constant $\bar{k}$. $\phi = 100$. At $k = \tau/\Delta\ell_0$, we can no longer approximate $\Delta\ell$ as being k independent. It decays like $k^{-1/3}$, leading to the shift to $\bar{k}^{2/3}$ growth in $\Delta\phi$.

paper, however, we will be concerned with the case where $u_p(0)$ is sampled from the equilibrium ensemble.

We begin our analysis with the long-time or equilibrium limit. We implement the long-time limit by removing the initial condition and setting the lower limit of integration to $-\infty$. This gives the long-time limit PIDE

$$\frac{d\Lambda}{dt} = \mathrm{D}\ell \sum_p p^2 \int_{-\infty}^{t} e^{-2\mathrm{D}\gamma_p^0(t-t') - 2\mathrm{D}kp^2[\Lambda(t)-\Lambda(t')]} dt'. \quad \text{(B5)}$$

In the long-time limit, we expect the system to reach equilibrium. Accordingly, we seek a solution of the form $\Lambda(t) = \lambda_0 t$, i.e., constant $\lambda_0(t)$. $\chi_q(t,t')$ then depends only on the time difference $(t-t')$, and we are free to Fourier transform. The right hand side of the PIDE can be viewed as the Fourier transform of $\tilde{\chi}_q^2(t,0)\Theta(t)$ evaluated at zero frequency, which leads us immediately to Eq. (46).

As expected, this reproduces the equilibrium mean-field theory equation of Ref. [13]. While, the sum can be performed in closed form, we approximate the summation by an integration in order to understand its k dependence. Since deviations in λ_0 from the spring-free result occur at larger values of k, the distinction between the summation and integration is immaterial. In terms of the k-independent change in projected length $\lambda_0^{\mathrm{free}}$ [found by setting $k = 0$ in Eq. (46)], we find the equation

$$\frac{\lambda_0}{\lambda_0^{\mathrm{free}}} = \left[1 + \frac{k\lambda_0^{\mathrm{free}}}{\tau}\left(\frac{\lambda_0}{\lambda_0^{\mathrm{free}}}\right)\right]^{-1/2}. \quad \text{(B6)}$$

The most interesting result is found at high k, where the solution to this equation demands $\lambda_0/\lambda_0^{\mathrm{free}} \sim k^{-1/3}$. Consequently, the effective tension $k\lambda_0 \sim k^{2/3}$. The transition occurs when $k\lambda_0/\tau \approx 1$. These results are confirmed by Fig. 11.

We now consider the short-time limit, where the behavior is dependent on the initial condition. We treat the case where $u_p(0)$ is averaged over the $k \neq 0$ equilibrium ensemble, and at $t = 0$ a small, additional time-dependent tension

$$\tau(t) = \tau + \delta f(t)\Theta(t) \quad \text{(B7)}$$

is applied. For reference, in equilibrium

$$\langle u_p^2(0)\rangle_{\mathrm{eq}} = \frac{2k_{\mathrm{B}}T/\ell}{\kappa p^2(p^2 + \tau + k\lambda_0)}, \quad \text{(B8)}$$

which can be inferred from the long-time MFT solution. $\delta f(t)$ has magnitude f, and is superimposed on top of a prestress τ. In analogy with defining the time-integrated projected length, we find it useful to introduce the time-integrated applied tension:

$$\delta F(t) = \int_0^t \delta f(t')dt'. \quad \text{(B9)}$$

Upon turning on the additional tension $\delta f(t)$, the projected length will change by an amount $\delta\langle\Delta\ell(t)\rangle = \langle\Delta\ell(t) - \Delta\ell(0)\rangle$, and the integrated projected length will change by an amount $\Lambda(t) = \Lambda_0 + \delta\Lambda(t)$, where $\Lambda_0 = \lambda_0^{\infty} t$ is the long-time constant solution. Comparing the two, we can identify

$$\partial_t \delta\Lambda = \delta\langle\Delta\ell\rangle. \quad \text{(B10)}$$

This relates $\delta\Lambda$ to the projected length response (which is not necessarily linear). Decomposing $\Lambda = \Lambda_0 + \delta\Lambda$, we redefine

$$\tilde{\chi}_q(t,t') = e^{-Dq^2(\kappa q^2 + \tau + k\lambda_0)(t-t')} e^{-Dq^2[\delta A(t) + \delta A(t')]}, \quad \text{(B11)}$$

where we have grouped the two perturbations $\delta\Lambda(t)$ and $\delta F(t)$ into a single function:

$$\delta\mathrm{A}(t) = k\delta\Lambda(t) + \delta F(t). \quad \text{(B12)}$$

This can similarly be accomplished by setting $\tau \to \tau + k\lambda_0 + \delta f(t)$ and replacing $\Lambda(t) \to \delta\Lambda(t)$ in Eq. (B3). Substituting and averaging over the initial condition yields the PIDE

$$\frac{d\delta\Lambda}{dt} = \frac{k_{\mathrm{B}}T}{2} \sum_q \left\{ \frac{\tilde{\chi}_q^2(t,0) - 1}{\kappa q^2 + \tau + k\lambda_0} + \frac{2q^2}{\xi_\perp} \int_0^t \tilde{\chi}_q^2(t,t')dt' \right\}. \quad \text{(B13)}$$

We are interested in the short-time solution to this equation. Since the projected length must be finite at $t = 0$, this implies that, at short times, $\delta\Lambda(t) \sim t^{\eta}$ for some $\eta > 1$. The prestress ensures that $\delta F(t)$ can be made small (by reducing the amplitude of applied tension) relative to τ at all values q, allowing one to expand $\delta F(t)$ in the exponential of $\tilde{\chi}_q(t,t')$ as $t \to 0$ [41]. Consequently, the change $\delta\Lambda(t)$ will be small as well, since it vanishes at $f = 0$. These considerations suggest that we can expand $\tilde{\chi}_q(t,t')$ in a power series about $\delta\Lambda(t)$ and $\delta F(t)$. Doing so, we find

$$\frac{d\delta\Lambda}{dt} = -\int_0^t M(t-t')[k\delta\Lambda(t') + \delta F(t')]dt', \quad \text{(B14)}$$

where we have defined the kernel

$$M(t) = \sum_p \left[\frac{\mathrm{D}p^2\delta(t)}{\kappa p^2 + \tau + k\lambda_0} - 2\mathrm{D}^2 p^4 e^{-2Dp^2(\kappa p^2 + \tau + k\lambda_0)t} \right]. \quad \text{(B15)}$$

This may be solved by Laplace transformation. The Laplace transform of the kernel is

$$\tilde{M}(z) = \sum_p \frac{z\mathrm{D}p^2}{(\kappa p^2 + \tau + k\lambda_0)[z + 2\mathrm{D}p^2(\kappa p^2 + \tau + k\lambda_0)]}. \quad \text{(B16)}$$

In terms of the dimensionless tension ϕ, the shift $\Delta\phi$ defined in Eq. (34), $\bar{k}$, and the dimensionless Laplace variable $\bar{z} = z\ell^4/D\kappa\pi^4$, we can equivalently write this as

$$\tilde{M}(\bar{z}) = \sum_{n=1}^{\infty} \frac{\mathrm{D}n^2\bar{z}/\kappa}{(n^2+\phi+\Delta\phi)[\bar{z}+2n^2(n^2+\phi+\Delta\phi)]}. \tag{B17}$$

Solving, the transformed change in projected length $\delta\Lambda(z)$ is

$$\delta\Lambda(z) = -\frac{\tilde{M}(z)/z}{1+k\tilde{M}(z)/z}\delta F(z). \tag{B18}$$

Since $F(z)$ is proportional to f, we may divide both sides by f, then use Eq. (B10) to obtain the Laplace transform of the projected length linear response:

$$\chi_{\Delta\ell}(z) = -z\frac{\tilde{M}(z)/z}{1+k\tilde{M}(z)/z}\frac{\delta F(z)}{f}. \tag{B19}$$

APPENDIX C: POLARIZATION FUNCTION CALCULATION

It is computationally easier to begin by working in the time domain. We decompose $\mathbf{M}^{-1}(t,t')$ in terms of its $k=0$ and $k\neq 0$ pieces via

$$\mathbf{M}^{-1}(t,t') = \boldsymbol{\sigma} + \mathrm{D}k\boldsymbol{\Pi}(t,t'), \tag{C1}$$

where $\boldsymbol{\sigma}$ represents the 2×2 block matrix with zeros along the diagonal, and identity matrices on the off diagonal. We call the additional contribution, $\boldsymbol{\Pi}(t,t')$, the polarization matrix, in analogy to electron screening in metals [34]. It encodes fluctuation corrections, and is determined by the trace log. Specifically, it is given by the second-order term in the Taylor expansion of $\mathrm{Tr}\ln(\mathbb{1}+Dkp^2\hat{G}\delta\hat{\lambda})$ about the small matrix

$$\delta\hat{\lambda}(t) = \begin{pmatrix} 0 & \delta\lambda(t) \\ \delta\lambda(t) & -\delta\bar{\lambda}(t) \end{pmatrix}. \tag{C2}$$

$\hat{G}$ is the saddle-point, matrix-valued Green's function

$$\hat{G}(t,t') = \begin{pmatrix} 0 & \bar{G}_p^-(t-t') \\ \bar{G}_p^+(t-t') & \bar{C}_p(t-t') \end{pmatrix}, \tag{C3}$$

with components given by the time representation of Eq. (58a),

$$\bar{G}_p^{\pm}(t) = \Theta(\pm t)e^{\mp D\gamma_p t}, \tag{C4}$$

and Eq. (58b),

$$\bar{C}_p(t,t') = 2D\int d\tau G^+(t-\tau)G^-(\tau-t'). \tag{C5}$$

The modified function $\gamma_p = \gamma_p^0 + kp^2\lambda_0$ includes the saddle-point value λ_0. The logarithm of matrices is defined via its Taylor series, the quadratic term of which is $\frac{-1}{2}\mathrm{Tr}\hat{G}\delta\hat{\lambda}\hat{G}\delta\hat{\lambda}$. The factor of $1/2$ can be factored out, per the definition of $\boldsymbol{\Pi}$. Products of the form $\hat{G}^{\pm}(t)\hat{G}^{\pm}(-t)$ have vanishing support due to the θ functions and are zero. Carrying out the matrix products, we find that $\boldsymbol{\Pi}(t,t') = \boldsymbol{\Pi}(t-t')$ is a function only of the time difference, with the result

$$\boldsymbol{\Pi}(t) = \sum_p p^4 \begin{pmatrix} -C_p^2(t) & 2G_p^+(t)C_p(t) \\ 2G_p^-(t)C_p(t) & 0 \end{pmatrix}. \tag{C6}$$

Since each of the operators depends on only the time difference $t-t'$, we may Fourier transform to frequency space. Including the $\boldsymbol{\sigma}$ contribution we find the effective functional matrix

$$\mathbf{M}_\omega^{-1} = \begin{pmatrix} -\Pi_\omega^0 & \Pi_\omega^+ + 1 \\ \Pi_\omega^- + 1 & 0 \end{pmatrix}. \tag{C7}$$

The individual components are given by Eqs. (61) and (62). We have chosen the $\pm$ notation to emphasize the similarity of $\Pi^{\pm}$ to Green's functions, and Π^0 to the spring-free correlator. Indeed, $\Pi^+ = (\Pi^-)^*$, and, as a consequence of the fluctuation-dissipation, the Π functions obey the relationship

$$\mathrm{Im}\Pi_\omega^+ = \frac{\omega}{2k_\mathrm{B}T}\Pi_\omega^0. \tag{C8}$$

We thus need only compute Π^+ to fully specify the polarization matrix.

APPENDIX D: TRANSVERSE SPRING ONLY

For completeness, we report the solution of the problem for a purely transverse spring attached at the end point (i.e., no longitudinal component). To incorporate both the longitudinal and transverse springs simultaneously, we simply replace the decay rates below with those calculated in the main text in the presence of a longitudinal spring. We follow the method of Ref. [13] for dealing with inhomogeneous boundary conditions in Fourier space. In this section, primes refer to spatial derivatives.

The homogeneous boundary conditions are pinned, with zero torque at both end points: $u(x_S) = u''(x_S) = 0$ and $x_S = 0, \ell$. Wave numbers are set to $p_n = n\pi/\ell$, for n a positive integer. The transverse spring replaces the pinned boundary condition $u(\ell)=0$ with the new condition

$$-\kappa u''''(\ell) + \tau u''(\ell) = -k_\perp u(\ell). \tag{D1}$$

In the bulk, we still have the linear Langevin equation

$$\partial_t u + \mathrm{D}\kappa u'''' - \mathrm{D}\tau u'' = \zeta(x,t), \tag{D2}$$

subject to the aforementioned boundary conditions. In order to implement the boundary condition, we add an additional force operator that is nondiagonal in wave number and regulated by a parameter ϵ that we take to zero at the end of the calculation [13]. We write

$$\left[\delta_{nm}\left(\partial_t + \mathrm{D}\kappa p_n^4 + \mathrm{D}\tau p_n^2\right) + \frac{1}{4\epsilon}\psi_n\psi_m\right]u_m = \delta_{nm}\xi_m, \tag{D3}$$

where we have defined the infinite dimensional vector

$$\psi_n = (-1)^n\left(\frac{\gamma_n}{p_n} + \frac{1}{2}k_\perp \sin 2n\pi\right). \tag{D4}$$

This is solved by the method of Green's functions. We replace ζ on the right side with a δ function in time and a Kronecker delta δ_{nk}, and $u_m(t)$ by the Green's function $\chi_{mk}^\perp(t-t')$. The response is still given by a sum over sines:

$$\chi^\perp(x,x';t) = \sum_{m,n=1}^{\infty}\chi_{mn}^\perp(t)\sin(p_n x)\sin(p_m x'). \tag{D5}$$

Next, we Laplace transform the χ version of Eq. (D3), take the inverse of the left side, and finally take the $\epsilon\to 0$ limit to

find

$$\chi^{\perp}_{mk}(s) = \chi^{\mathrm{D}}_{mk}(s) + \chi^{\mathrm{BC}}_{mk}(s), \tag{D6}$$

which has decomposed into a homogeneous part plus boundary term. The homogeneous part is

$$\chi^{\mathrm{D}}_{nm}(s) = \chi^{0}_{n}(s)\delta_{nm} = \frac{\delta_{nm}}{s+\gamma_n}, \tag{D7}$$

where for this section we have defined

$$\gamma_n = D\kappa p_n^4 + D\tau p_n^2. \tag{D8}$$

The boundary term is given by

$$\chi^{\mathrm{BC}}_{mk}(t) = \frac{-\left(\chi^{0}_{n}\psi_n\right)^2}{\sum_{n=1}^{\infty}\psi_n\chi^{0}_{n}\psi_n}. \tag{D9}$$

The numerator is

$$\text{numerator} = -\frac{(-1)^{n+m}}{p_n p_m}\left[\frac{\gamma_n\gamma_m}{(s+\gamma_n)(s+\gamma_m)}\right]. \tag{D10}$$

The denominator is a divergent sum. It has two main pieces:

$$\sum_{n=1}^{\infty}\left\{\frac{\gamma_n^2}{p_n^2(s+\gamma_n)} + k_{\perp}\frac{\gamma_n \sin 2\pi n}{p_n(s+\gamma_n)} + \text{convergent}\right\}. \tag{D11}$$

The third piece is a convergent sum proportional to $\sin 2\pi$, and can be safely set to zero. We rewrite the series by subtracting out the divergent pieces as

$$\sum_{n=1}^{\infty}\left\{\frac{-s\gamma_n}{p_n^2(s+\gamma_n)} + \frac{\gamma_n}{p_n^2} + \frac{-s\sin 2\pi n}{p_n(s+\gamma_n)} + \frac{k_{\perp}\sin 2\pi n}{p_n}\right\}. \tag{D12}$$

The first and third are now convergent, so the third can immediately be set to zero. The second and fourth need regularization. These sums were computed previously [13], with the results $-\tau/2$ and $-k_{\perp}\ell/2$, respectively. We then have

$$\text{denominator} = -\frac{1}{2}(\tau + k_{\perp}\ell) - \sum_{n=1}^{\infty}\frac{s\left(\kappa p_n^2 + \tau\right)}{s + \kappa p_n^4 + \tau p_n^2}. \tag{D13}$$

Combining, we find the boundary response

$$\chi^{\mathrm{BC}}_{mn}(s) = \frac{2(-1)^{n+m}\gamma_n\gamma_m}{p_n p_m(\tau + k_{\perp}\ell + F(s))(s+\gamma_n)(s+\gamma_m)}, \tag{D14}$$

where

$$F(s) = 2\sum_{n=1}^{\infty}\frac{s\left(\kappa p_n^2 + \tau\right)}{s + \kappa p_n^4 + \tau p_n^2}. \tag{D15}$$

The sum of Eqs. (D7) and (D14) gives the final result for the Laplace-transformed response function for a purely transverse spring at the boundary. To obtain the space-time domain solution, one can numerically perform the inverse transform and sum over modes according to Eq. (D5).

[1] R. H. Pritchard, Y. Y. S. Huang, and E. M. Terentjev, Soft Matter **10**, 1864 (2014).
[2] C. P. Broedersz and F. C. MacKintosh, Rev. Mod. Phys. **86**, 995 (2014).
[3] D. T. Chen, Q. Wen, P. A. Janmey, J. C. Crocker, and A. G. Yodh, Annu. Rev. Condens. Matter Phys. **1**, 301 (2010).
[4] C. Heussinger, B. Schaefer, and E. Frey, Phys. Rev. E **76**, 031906 (2007).
[5] P. Fernández, S. Grosser, and K. Kroy, Soft Matter **5**, 2047 (2009).
[6] P. A. Janmey, M. E. McCormick, S. Rammensee, J. L. Leight, P. C. Georges, and F. C. MacKintosh, Nat. Mater. **6**, 48 (2007).
[7] H. Kang, Q. Wen, P. A. Janmey, J. X. Tang, E. Conti, and F. C. MacKintosh, J. Phys. Chem. B **113**, 3799 (2009).
[8] F. Gittes, B. Schnurr, P. D. Olmsted, F. C. MacKintosh, and C. F. Schmidt, Phys. Rev. Lett. **79**, 3286 (1997).
[9] F. Gittes and F. C. MacKintosh, Phys. Rev. E **58**, R1241(R) (1998).
[10] R. Granek, J. Phys. II **7**, 1761 (1997).
[11] D. C. Morse, Phys. Rev. E **58**, R1237(R) (1998).
[12] E. N. Lissek, T. F. Bartsch, and E.-L. Florin, bioRxiv (2018), doi: 10.1101/382903.
[13] J. Kernes and A. J. Levine, Phys. Rev. E **101**, 012408 (2020).
[14] A. J. Levine, D. Head, and F. C. MacKintosh, J. Phys.: Condens. Matter **16**, S2079 (2004).
[15] D. A. Head, A. J. Levine, and F. C. MacKintosh, Phys. Rev. E **72**, 061914 (2005).
[16] C. Heussinger and E. Frey, European Phys. J. E **24**, 47 (2007).
[17] M. J. Grill, J. Kernes, V. M. Slepukhin, W. A. Wall, and A. J. Levine, arXiv:2006.15192.
[18] D. Mizuno, C. Tardin, C. F. Schmidt, and F. C. MacKintosh, Science **315**, 370 (2007).
[19] F. C. MacKintosh and A. J. Levine, Phys. Rev. Lett. **100**, 018104 (2008).
[20] D. Mizuno, D. Head, F. MacKintosh, and C. Schmidt, Macromolecules **41**, 7194 (2008).
[21] A. J. Levine and F. MacKintosh, J. Phys. Chem. B **113**, 3820 (2009).
[22] L. Starrs and P. Bartlett, J. Phys.: Condens. Matter **15**, S251 (2002).
[23] K. M. Addas, C. F. Schmidt, and J. X. Tang, Phys. Rev. E **70**, 021503 (2004).
[24] O. Latinovic, L. A. Hough, and H. D. Ou-Yang, J. Biomech. **43**, 500 (2010).
[25] U. C. Täuber, *Critical Dynamics: A Field Theory Approach to Equilibrium and Non-Equilibrium Scaling Behavior* (Cambridge University, Cambridge, England, 2014).
[26] F. C. MacKintosh, J. Käs, and P. A. Janmey, Phys. Rev. Lett. **75**, 4425 (1995).
[27] O. Hallatschek, E. Frey, and K. Kroy, Phys. Rev. Lett. **94**, 077804 (2005).

[28] O. Hallatschek, E. Frey, and K. Kroy, Phys. Rev. E **75**, 031905 (2007).
[29] O. Hallatschek, E. Frey, and K. Kroy, Phys. Rev. E **75**, 031906 (2007).
[30] C. H. Wiggins, D. Riveline, A. Ott, and R. E. Goldstein, Biophys. J. **74**, 1043 (1998).
[31] E. Farge and A. C. Maggs, Macromolecules **26**, 5041 (1993).
[32] J. Lighthill, SIAM Rev. **18**, 161 (1976).
[33] P. C. Hohenberg and B. I. Halperin, Rev. Mod. Phys. **49**, 435 (1977).
[34] A. Altland and B. D. Simons, *Condensed Matter Field Theory* (Cambridge University, Cambridge, England, 2010).
[35] J. Rammer, *Quantum Transport Theory* (CRC, Boca Raton, FL, 2018).
[36] J. M. Ziman, *Models of Disorder: The Theoretical Physics of Homogeneously Disordered Systems* (Columbia University, New York, 1979).
[37] J. Zinn-Justin, *Quantum Field Theory and Critical Phenomena* (Clarendon, Oxford, 1996).
[38] U. Seifert, W. Wintz, and P. Nelson, Phys. Rev. Lett. **77**, 5389 (1996).
[39] R. Everaers, F. Jülicher, A. Ajdari, and A. C. Maggs, Phys. Rev. Lett. **82**, 3717 (1999).
[40] T. Hiraiwa and T. Ohta, J. Phys. Soc. Jpn. **77**, 023001 (2008).
[41] B. Obermayer and E. Frey, Phys. Rev. E **80**, 040801(R) (2009).
[42] The response of unstressed filaments in an equilibrium ensemble to an applied tension at $t = 0$ has been studied [10,28], and incorrectly extended to filament fluctuations under prestress via the fluctuation dissipation theorem [2]. The response is not in the linear forcing regime, and thereby the fluctuation dissipation theorem does not hold.
[43] K. C. Neuman and S. M. Block, Rev. Sci. Instrum. **75**, 2787 (2004).